INFLUENCE OF RELATIVE DENSITY AND MICROSTRUCTURAL ANISOTROPY ON THE GLOBAL ELASTIC PROPERTIES OF CELLULAR STRUCTURES

by

JUSTIN COMPTON

Presented to the Faculty of the Graduate School of

The University of Texas at Arlington in Partial Fulfillment

of the Requirements

for the Degree of

MASTER OF SCIENCE IN AEROSPACE ENGINEERING

THE UNIVERSITY OF TEXAS AT ARLINGTON

May 2017

Supervising Committee:

Ashfaq Adnan (Supervising Professor)

Wen S Chan

Robert M Taylor

Acknowledgements

I am immensely fortunate to have Dr. Ashfaq Adnan as my advisor. I would like to thank him for his invaluable support, guidance, and accessibility throughout the course of my research. As a distance education student, he welcomed me into the UTA family. I would like to thank Dr. Wen Chan and Dr. Robert Taylor for graciously serving on my advisory committee. I am thankful for the Department of Mechanical and Aerospace Engineering at UTA, especially Debi Barton. She made the challenges and complexities associated with being a distance education student manageable.

I greatly appreciate L3 Mission Integration for generously funding my graduate studies through their educational assistance program.

I would like to thank my parents who always encouraged me to pursue my goals with passion and discipline. My accomplishments are attributed to their love and support. I would also like to thank Courtney for her patience and encouragement.

April 26, 2017

Abstract

INFLUENCE OF RELATIVE DENSITY AND MICROSTRUCTURAL ANISOTROPY ON THE GLOBAL ELASTIC PROPERTIES OF CELLULAR STRUCTURES

Justin Compton, M.S.

The University of Texas at Arlington, 2017

Supervising Professor: Ashfaq Adnan

The favorable strength-to-weight ratio of cellular solids makes them ideal for structural applications. With the advent of additive manufacturing, the fabrication of complex cellular structures is becoming a reality. It is therefore necessary to understand the mechanical properties of cellular structures. The global mechanical properties of cellular structures are governed by geometry and therefore, differ from the mechanical properties of the base material from which they are constructed. In this study, finite element models are developed to explore the effective elastic properties of honeycomb structures for isotropic and anisotropic microstructural material properties. Finite element models are generated for regular, hexagonal honeycombs and irregular, Voronoi honeycombs to study the relationship between cell regularity and microstructural anisotropy. Lastly, the finite element models vary in relative density from purely solid to purely cellular to better understand the ranges of relative densities where a structure behaves as a cellular structure versus a porous solid. The results of the finite element analysis are compared to the theoretical solutions for regular, hexagonal honeycombs as well as the theoretical solutions for porous media. A recommendation is made to the theoretical analysis of honeycombs to improve correlation with the finite element results.

Table of Contents

List of Illustrations

List of Tables

Chapter 1

Introduction

The favorable strength-to-weight ratio of cellular solids has captured the attention of engineers and manufacturers. In the aircraft industry, weight is directly proportional to fuel consumption, which is one of the largest operating expenses for aircraft [14]. The weight savings potential of cellular solids is already being utilized. Sandwich honeycomb panels are widely used in floor panels, sidewall panels, and equipment support structure. As advancements in manufacturing technology continue to unfold, industry leaders are expanding beyond honeycomb panels and are developing more complex cellular structures. For instance, The Boeing Company recently debuted a microlattice structure that they claim is the lightest metal ever made [30]. Not long ago, the fabrication of complex cellular solids was infeasible. Today, the advent of additive manufacturing allows designers to construct such geometries. With the implementation of cellular structures gaining momentum, it is necessary to understand their behavior and mechanical properties.

The global mechanical properties of cellular structures are governed by geometry and therefore, differ from the mechanical properties of the base material from which they are constructed. Their unique properties have been heavily researched and the literature is vast. With geometry playing a key role in the global mechanical properties, the influence of cellular geometry has been heavily studied. Previous research focuses on periodic unit cells of various geometries and the influence of cell size (i.e. relative density of the specimen). Dai et al. [9] studied the effective Young's modulus for periodic unit cells with rectangular, triangular, hexagonal, and trihexagonal geometries, each with varying cell sizes. Much more complex geometries have been studied including

hierarchical honeycomb structures by Gandhi [18] and auxetic chiral structures by Joshi [28]. Irregular Voronoi honeycombs are a widely accepted means of generalizing the random and complex geometry of cellular solids found in nature, such as plant cells and trabecular bone. Gibson et al. [19], Silva et al. [38], and Zhu et al. [47] have extensively studied the role of regularity and relative density on the effective mechanical properties of Voronoi honeycombs.

A sector of the literature focuses on the macroscopic anisotropy of regular, hexagonal honeycombs and irregular, Voronoi honeycombs. It is interesting to note that the random cellular network of irregular honeycombs does not imply anisotropy. According to Gibson and Ashby [19], “Macroscopic anisotropy can arise from anything that, when averaged over a large number of cells, destroys hexagonal symmetry.” They list several contributors to macroscopic anisotropy such as: missing or broken cell walls, cell walls of unequal thickness, the orientation of cell walls aligning toward a preferred directions, and cell elongation. Each of the aforementioned sources of anisotropy has received some attention. Chen et al. [6] studied the effects of cell wall waviness, non-uniform wall thickness, fractured cell walls, missing cell walls, and cell wall misalignments for biaxial loading scenarios. Silva and Gibson [37] investigated the effects of missing cell walls on the compressive strength for both regular and irregular honeycombs. Silva et al. [38] studied the effects of cell elongation.

The macroscopic anisotropy of honeycombs has been limited to the study of geometry and has not focused on the anisotropic material properties of the solid material. Cellular structures are typically formed via a foaming process where gas bubbles nucleate and grow to form a random network of voids. The disadvantage to this method is that it can only create random Voronoi structures. Conversely, additive manufacturing allows the manufacturer to design and fabricate specific geometric networks. Objects

fabricated using additive manufacturing processes are inherently anisotropic. Complex thermal cycles of the layer-by-layer stack up, porosity, and lack of fusion are just a few of the variables that produce anisotropic microstructures. Analyses of the mechanical properties of materials fabricated by direct energy deposition processes, both powder and wire fed, have shown that the tensile strengths along the travel direction can be up to 20 percent higher than the tensile strength along the build direction [35, 43, 44]. Therefore, it is expected that microstructural anisotropy impacts the effective mechanical properties of cellular structures.

In this study, Finite Element Models (FEMs) are developed to explore the effective mechanical properties of honeycomb structures for isotropic and anisotropic microstructural material properties. FEMs are generated for regular, hexagonal honeycombs and irregular, Voronoi honeycombs to study the relationship between cell regularity and microstructural anisotropy. Lastly, the FEMs vary in relative density from purely solid to purely cellular to better understand the ranges of relative densities where a structure behaves as a cellular structure versus a porous solid.

Chapter 2

Modeling Voronoi Honeycombs

In addition to additive manufacturing processes, cellular solids can be created by the nucleation and growth of cells. If the cells nucleate randomly and simultaneously in two dimensions, and grow radially at the same linear rate, then the resulting structure is a random Voronoi honeycomb (random Voronoi foam for three dimensions) [38]. According to Gibson and Ashby [19], several types of metal foams are manufactured via a foaming process where a supersaturated gas separates from a liquid. The gas initially takes the form of spherical bubbles. As the spheres grow, they interact with neighboring spheres to form polyhedral cells. An example of such structure is depicted in Figure 2-1(a) for the cross-sectional view of the core of an aluminum foam sandwich. The figure is modified in Figure 2-1(b) to illustrate the polygonal representation of cells.

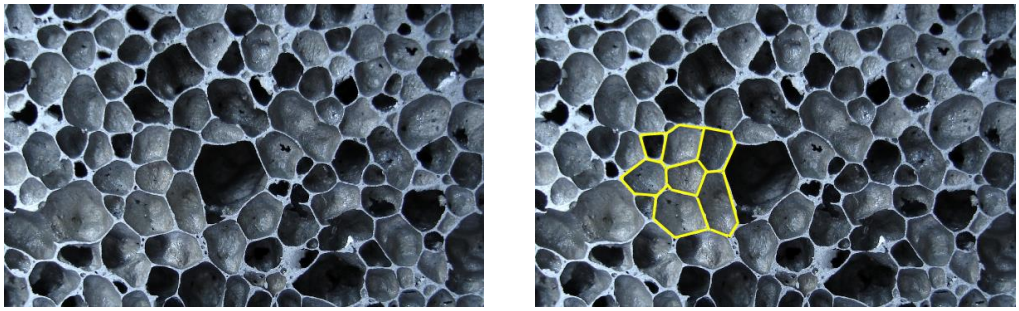

(a) (b)

Figure 2-1 (a) Core of an aluminum foam sandwich [32]; (b) polygonal representation of cell walls

The initial bubbles can be considered as randomly generated points in space. In probability theory, there exist numerous methods for the generation of spatial point arrangements. For the present thesis, points are randomly produced via the Simple Sequential Inhibition (SSI) process.

2.1 Geometric Methods

2.1.1 Simple Sequential Inhibition Process

The Simple Sequential Inhibition (SSI) process belongs to a family of models used in packing or space filling problems [5]. The SSI process states that for a finite area *A*, disks of unit diameter *d* are sequentially generated at random within the prescribed boundary [12]. Each new disk is uniformly generated independent of all preceding disks. The SSI process requires that no two disks overlap; thus, if two disks overlap, then the newly created disk is rejected and another random disk is generated. The procedure terminates when the desired number *n* of disks has been generated or when no further disks can be added. The final distribution of points is defined by the disk centers.

The SSI process employed in this thesis slightly differs from the method previously described in that the entire disk need not fit within the prescribed boundary. It is only necessary that the disk center is within the prescribed boundary. As a result, the disk center may be located along a boundary.

The disk diameter *d* is commonly referred to as the inhibition distance since it restricts the location of subsequent disks (i.e. points). When the inhibition distance is relatively small, a highly irregular arrangement of points ensues. As the inhibition distance increases, the arrangement of points becomes more regular. This trend was demonstrated by Gálvez [16] who generated 100 points within a one unit square area with inhibition distances of $d = 0$, $d = 0.05$, and $d = 0.1$. Gálvez's demonstration is recreated in Figure 2-2 with inhibition distances of (a) $d = 0$, (b) $d = 0.04$, and (c) $d = 0.08$.

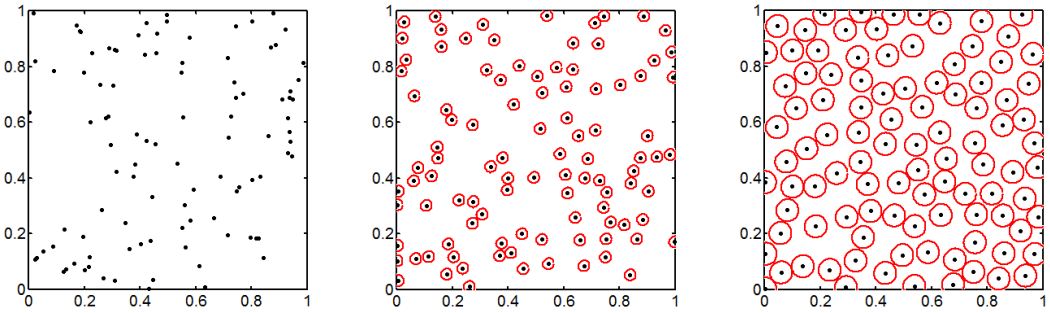

Figure 2-2 Planar point patterns for n = 100 in a unit square with inhibition distance (a) *d* = 0, (b) *d* = 0.04, (c) *d* = 0.08 (recreated from Gálvez [16])

The red circles represent the disk perimeters and the black points the disk centers. Figure 2-2 reveals that packing density η is the essential parameter of the SSI process,

$$\eta = \frac{n\pi d^2}{4A} \tag{1}$$

which is the fraction of finite area *A* covered by quantity *n* non-overlapping disks of diameter *d* [11, 12]. As the disk diameter increases, the placement of disks becomes increasingly restrictive. As a result, the packing of disks is more orderly. It is apparent that there is some packing arrangement that produces a maximum packing density. Such an arrangement occurs when each disk center is located at a distance equal to its diameter *d* from its neighbors. Illustrated in Figure 2-3, common examples of this stacking sequence include staggered stacking of pipe for efficient storage and transport and staggered bundling of wires for wire routing applications.

Figure 2-3 Maximum packing density of (a) pipes [41], (b) wire bundles [15]

Figure 2-3 clearly shows that the maximum packing density occurs when each disk is surround by six other disks, i.e., when the disk centers are arranged in a hexagonal lattice. The hexagonal lattice arrangement has a packing density of

$$\eta = \frac{\pi}{2(3)^{1/2}} \tag{2}$$

With the finite area *A* and the number of disks *n* known, the maximum distance between two adjacent points d_{max} is derived by substituting equation (2) into equation (1).

$$d_{max} = \left(\frac{2A}{n(3)^{1/2}}\right)^{1/2} \tag{3}$$

Zhu [47] affirms that d_{max} is the maximum disk diameter and that the specified inhibition distance *d* must be less than or equal to d_{max}. If *d* is greater than d_{max}, then it will not be possible to place all *n* disks within the finite area *A*. Zhu then defines the following regularity parameter:

$$\delta = \frac{d}{d_{max}} \tag{4}$$

where $\delta = 1$ (i.e. $d = d_{max}$) represents a regular arrangement of points and $\delta = 0$ (i.e. $d = 0$) represents an entirely random arrangement of points.

2.1.2 Voronoi Diagram

Once the spatial arrangement of points has been defined, a classical Voronoi diagram may be constructed. Aurenhammer and Klein [2] have thoroughly defined the mathematical properties governing Voronoi diagrams. For convenience, their mathematical definition is reiterated here. Let a set *S* of *n* points *p, q,…* be defined in the plane. For points *p* and *q* belonging to *S*, the perpendicular bisector of the line segment $\overline{pq}$ is defined as

$$B(p,q) = \{x \mid d(p,x) = d(q,x)\} \tag{5}$$

The perpendicular bisector *B(p,q)* separates the halfplane containing *p*

$$D(p,q) = \{x \mid d(p,x) < d(q,x)\} \tag{6}$$

from the halfplane containing *q*

$$D(q,p) = \{x \mid d(q,x) < d(p,x)\} \tag{7}$$

The Voronoi cell of *p* with respect to *S* is then defined as

$$VR(p,S) = \bigcap_{q \in S, q \neq p} D(p,q) \tag{8}$$

Lastly, the Voronoi diagram of *S* is defined as

$$V(S) = \bigcup_{p,q \in S, p \neq q} \overline{VR(p,S)} \cap \overline{VR(q,S)} \tag{9}$$

Simply stated, the Voronoi diagram is obtained by constructing the perpendicular bisectors of the lines connecting each pair of adjacent points and trimming the bisectors where they intersect. Each Voronoi cell is the smallest cell containing the nucleation point while bounded by the bisectors (i.e. cell walls) [38, 47].

The lines connecting each pair of adjacent points are obtained via a Delaunay tessellation. The Delaunay tessellation is the process of creating line segments between nucleation points with the only requirement being that there exists a circle *C* that passes through the line endpoints while not encompassing any other nucleation point in its interior or boundary [2]. Development of the Delaunay tesselation (dashed blue lines) and the Voronoi diagram (solid black lines) is illustrated in Figure 2-4.

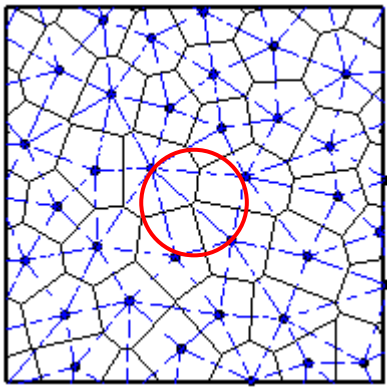

Figure 2-4 Voronoi diagram (solid black lines), Delaunay tessellation (dashed blue lines), and circular restraint (solid red circle)

Figure 2-4 confirms that no additional nucleation point is enclosed by a circle circumscribing the endpoints of a Delaunay tessellation. It is also noted that each Voronoi cell is the intersection of *n-1* halfplanes containing the respective nucleation point [2]. As a result, a Voronoi diagram is the decomposition of space into convex regions.

The Voronoi diagram discussed thus far is termed classical because it is in its simplest form. Classical Voronoi diagrams adhere to the assumptions that each cell contains its nucleation point and that each bisector contributes to one cell wall. However, it is important to acknowledge that these assumptions do not fully capture the true cellular geometry. For instance, the foam sandwich core presented in Figure 2-1(a) is revisited in Figure 2-5. Studying Figure 2-5 reveals several features that deviate from the classical Voronoi diagram such as curved cell walls, voids contained within the cell walls, cell walls of variable thickness, and missing cell walls. These natural variations are common results of the foaming process. In general, every cell wall has some degree of curvature due to the pressure difference between the neighboring cells [19]. Voids within the cell walls (i.e. small cells making up the walls of larger cells) are a consequence of growth rates unique to each cell. Specifically, cells containing a below average number of cell walls shrink, cells with an above average expand, and cells with an average number of sides remain

constant [19]. Competitive growth rates, surface tension, and the progressive generation of nucleation sites are just a few of the parameters that contribute to variability of cell wall thicknesses, as well as the omission of cell walls.

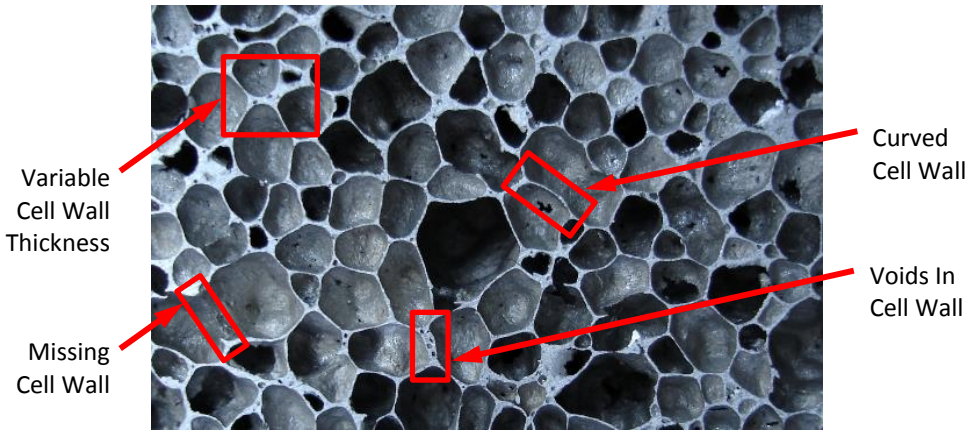

Figure 2-5 Natural variations observed in the core of an aluminum foam sandwich [32]

These natural variances can be captured by manually assigning wall thicknesses, deleting specific cell walls, and by modeling higher-order Voronoi diagrams. Higher-order Voronoi diagrams are useful in modeling complex arrangements because cells are not required to contain its nucleation point and bisectors are capable of producing more than one cell wall [2]. These complex arrangements have received attention [6, 21, 37]; however, they are beyond the scope of this thesis. The present thesis employs a classical Voronoi diagram with linear cell walls of uniform thickness and without any structural defects.

2.2 Geometric Development

The MATLAB® software package is employed for generating random points via the SSI process and performing the Voronoi partition. The SSI algorithm provided by Martinez and Martinez [31] is leveraged and then expanded upon to include the Voronoi partition. The aforementioned algorithm is presented in Appendix A. The algorithm inputs

include the boundary vertices *rx* and *ry*, the number of points *n* to be located within the boundary, and the inhibition distance *d*. It is desired that for a perfect arrangement of points (i.e. $\delta = 1$, hexagonal honeycomb), that the inhibition distance is equal to 42 units (i.e. d_{max} in equation (4)). This is equivalent to a hexagonal cell height of 42 units. Assuming a cell wall thickness of 1, the ratio of cell height to cell wall thickness is 42. This ratio is representative of a common honeycomb design manufactured by HEXCEL Corporation [25] where the foil thickness is 0.003 inches and the cell height is 0.125 inches. It is also preferred that the boundary contains a sufficient number of honeycomb cells. Onck et al. [34] studied the effects of the specimen size relative to the cell size on the elastic and shear moduli of regular, hexagonal honeycombs. Their tests revealed that the Young's modulus for smaller specimens drops significantly and that it converges to the bulk modulus for larger specimens. Conversely, the shear modulus peaks for smaller specimens, and it converges to the bulk modulus for larger specimens. They concluded that a specimen having at least 17 cells along its height and width is sufficient in minimizing boundary effects. To satisfy their requirement, and to ensure that the specimen is symmetric about the vertical and horizontal centerlines, it is decided that the boundary contains 20 rows and 21 columns of honeycomb cells. This equates to a specimen roughly 777 units in width, 840 units in height, and accommodating 430 nucleation points. As Gálvez [16] observes, the probability of generating a perfectly regular arrangement of points via the SSI process is extremely small since it requires that all points are randomly generated in the precise position of a regular arrangement. Therefore, the arrangement of points for $\delta = 1$ is generated by manually locating points at a distance of 42 units from its neighbors. For the irregular arrangement, a regularity of $\delta = 0.75$ is arbitrarily chosen. Referencing equation (4), this results in an inhibition distance of 31.5 units. The point patterns for $\delta = 1$ and $\delta = 0.75$ are shown in Figure 2-6.

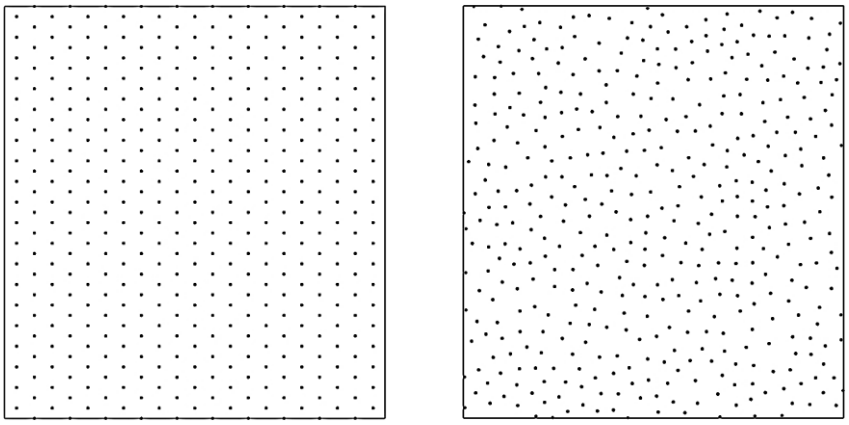

(a) (b)

Figure 2-6 Nuclei pattern with a regularity of (a) $\delta = 1.0$ and (b) $\delta = 0.75$

As stated in Section 2.1.2, a classical Voronoi diagram is constructed after the spatial arrangement of points is defined. The MATLAB® function `[v,c]=voronoin(X)` is used to perform the Delaunay tessellation and construct the Voronoi diagram; where *X* is the nuclei point array input, *v* is the Voronoi vertice array output, and *c* is the Voronoi cell array output. The Voronoi honeycombs, along with their respective point patterns, for $\delta = 1$ and $\delta = 0.75$ are presented in Figure 2-7.

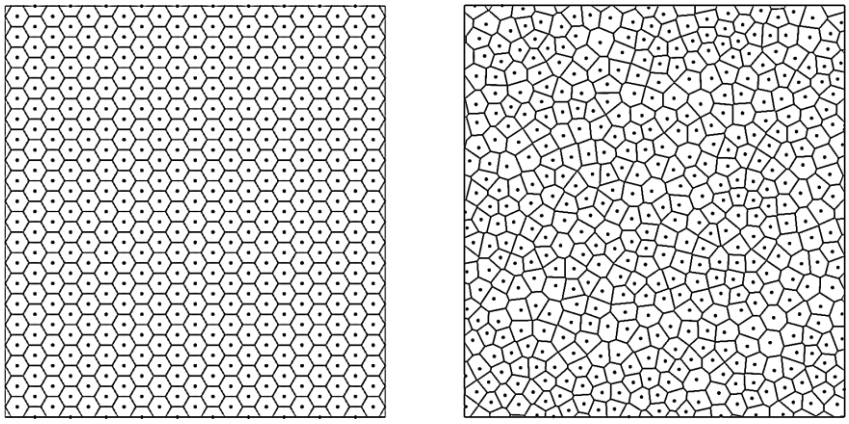

(a) (b)

Figure 2-7 Voronoi honeycomb with a regularity of (a) $\delta = 1.0$ and (b) $\delta = 0.75$

As expected, introducing irregularity also introduces significant variance in cell geometries. For Figure 2-7(b), the area of the largest cell is nearly 3 times that of smallest cell. When normalizing the cell areas so that the sum of all cell areas equates to 1, the standard deviation (i.e. cell dispersion) is 0.155; implying a moderate dispersion of cell sizes. However, it is interesting to note that the average cell size is nearly the same between both figures. The average cell area in Figure 2-7(a) is roughly 1528 square units and the average cell area in Figure 2-7(b) is about 1506 square units; a difference slightly over 1%.

Irregularity also influences the number of edges constituting a cell. For the arrangement in Figure 2-7(b), the cells range from 3 sides up to 12 sides. However, six sided cells are the most prevalent, as shown in Figure 2-8.

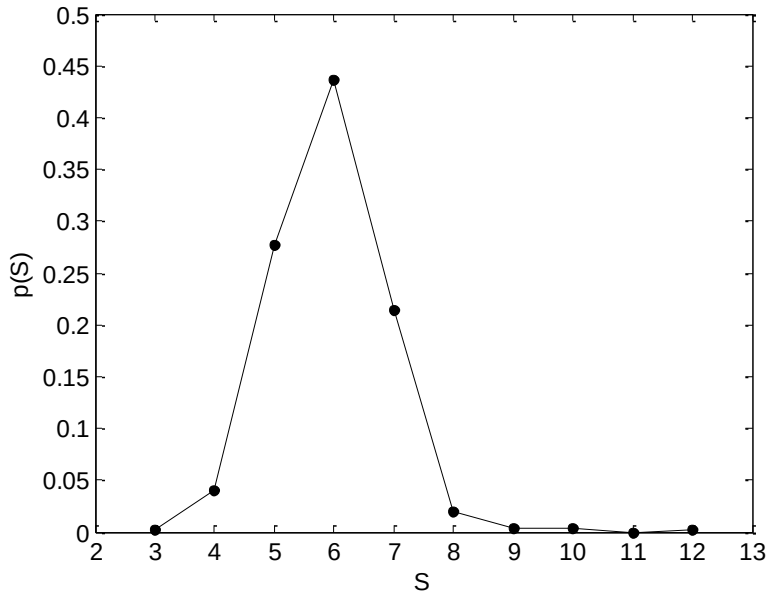

Figure 2-8 Probability *p(S)* of finding cells with side *S*

In addition to the high probability of 6 sided cells, the average number of sides per cell is also 6 in accordance with Euler's law [2, 19].

It is interesting to observe the Voronoi cells along the boundary in Figure 2-7. The cell walls are forced to terminate at the boundary and the boundary closes off the cell. Otherwise, the cell walls would extend to infinity in what is termed an unbounded cell. Referencing Section 2.1.2, each Voronoi cell is the intersection of *n-1* halfplanes containing the respective nucleation point. Investigating the cells along the boundary reveals that they lack a sufficient number of halfplanes to close off the cell. This is due to the absence of nucleation points beyond the boundary which results in the nucleation points near the boundary belonging to halfplanes that extend to infinity. Thus, cell walls extend to infinity. In actuality, majority of the cell walls will intersect and close off the cell. While the intersection points are not at infinity, they can be located well beyond the boundary such that they produce unrealistic cell geometries. An example of unbounded cells is provided in Figure 2-9.

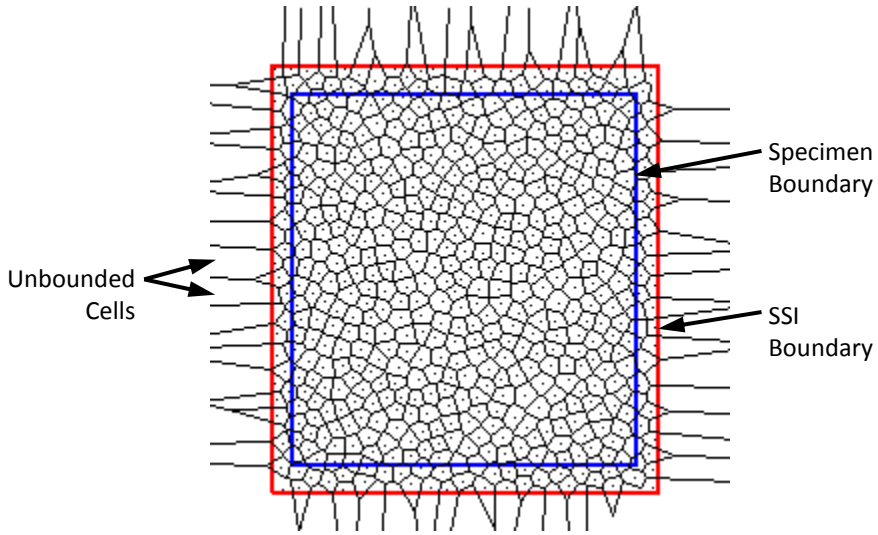

Figure 2-9 Unbounded Voronoi cells

In the above example, the red box denotes the boundary specified for the SSI process (reference Section 2.1.1) and the blue box designates the specimen boundary. As can be seen, nucleation points do not exist outside the SSI boundary which results in

unbounded cells. It is common practice to close off the Voronoi cells by constructing a simple closed curved that intersects only the unbounded cell edges [2, 16]. An example of such curve is the SSI boundary. Enforcing the SSI boundary to close off the cells yields abnormal cell geometries along the boundary. Therefore, it is the practice of the present thesis to define the SSI boundary sufficiently beyond the desired specimen boundary and then close off the cells with the specimen boundary; thus, achieving more realistic cell geometries. In addition to expanding the SSI boundary, the number of nucleation points n must be increased so that the density of points remains constant.

After creating the Voronoi partition in MATLAB®, the cell vertices are exported to Siemens NX™ for constructing the two-dimensional model geometries. The Siemens NX™ software package is a powerful computer-aided design (CAD) software program that includes several application programming interfaces (APIs) that allow the user to write programs to customize and enhance NX™. Therefore, the repetitive and time-consuming task of manually creating honeycomb cells via the graphical user interface (GUI) is replaced by a simple application. Specifically, the Simple NX Application Programming (SNAP™) API is employed to automate the process of generating the honeycomb cells. The SNAP™ code imports the cell vertices into Siemens NX™ and then proceeds to create line segments between the points. The complete SNAP™ code is provided in Appendix A.

Adding thickness to the line segments, i.e., cell walls, is conveniently achieved via the rib feature. Wall thicknesses are derived as a function of cell growth. It was stated earlier that the regular hexagonal arrangement has a total cell height 42 units. This is composed of an internal cell height h_w of 41 units and a wall thickness t_w of 1 unit. This geometry occurs when the cell is fully developed. To determine the wall thickness when the cell is 90% developed, 90% of 41 units is subtracted from the total cell height of

42 units. Using this methodology, cell wall thicknesses are calculated for cell growths ranging from 10% to 100% in increments of 10. The results are presented in Table 2-1.

Table 2-1 Relative densities for honeycomb with regularity δ = 1.0

Percent of Max Cell Height	Cell Height (h_w)	Cell Wall Thickness (t_w)	Relative Density ($\bar{\rho}$) for δ = 1.0
10	4.1	37.9	0.991
20	8.2	33.8	0.963
30	12.3	29.7	0.916
40	16.4	25.6	0.850
50	20.5	21.5	0.766
60	24.6	17.4	0.662
70	28.7	13.3	0.538
80	32.8	9.2	0.395
90	36.9	5.1	0.221
100	41.0	1	0.048

The relative density $\bar{\rho}$ is the density of the honeycomb ρ^* divided by the density of the solid ρ_s of which it is made. For two dimensions, the relative density is equivalent to area fraction. Figure 2-10 shows the honeycomb geometries for the relative densities listed in Table 2-1.

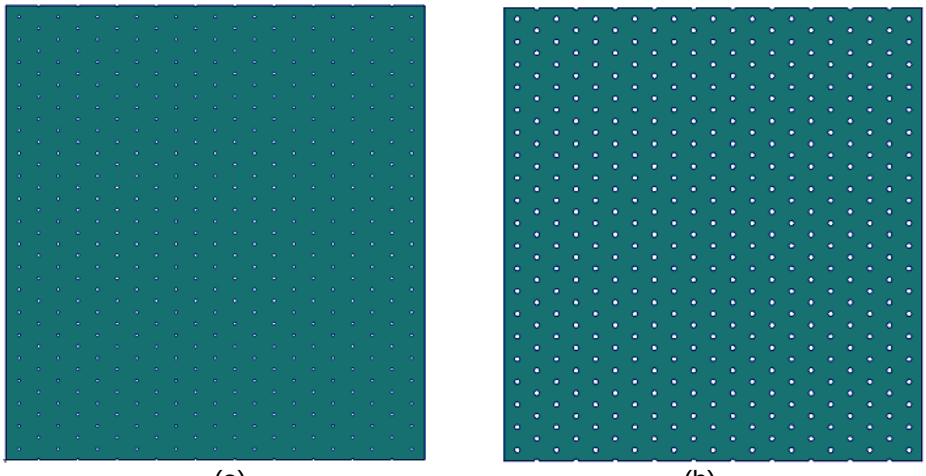

(a) (b)

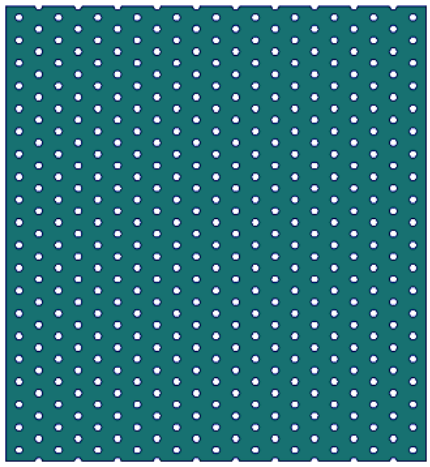

(c)

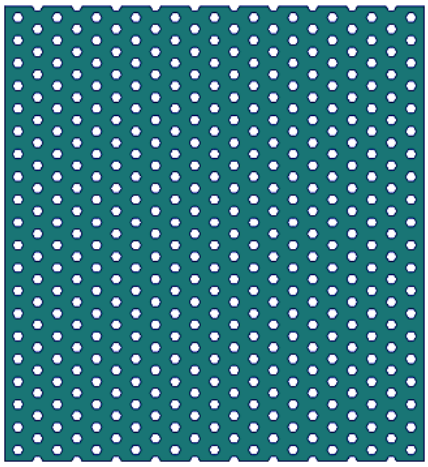

(d)

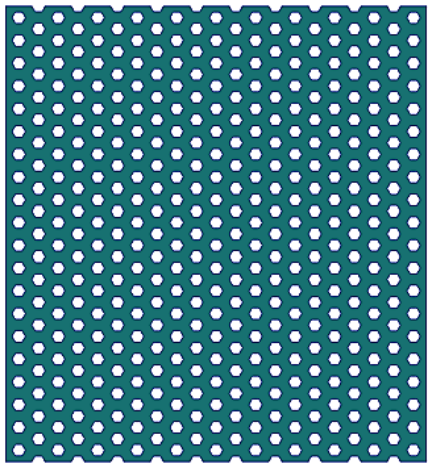

(e)

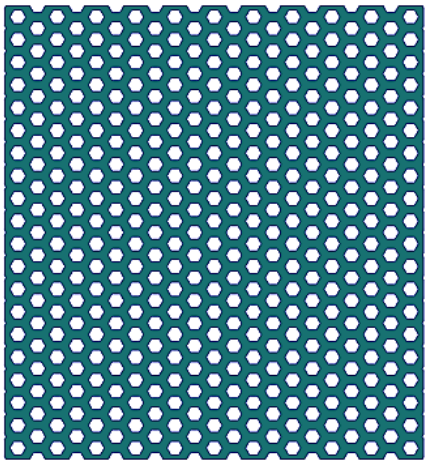

(f)

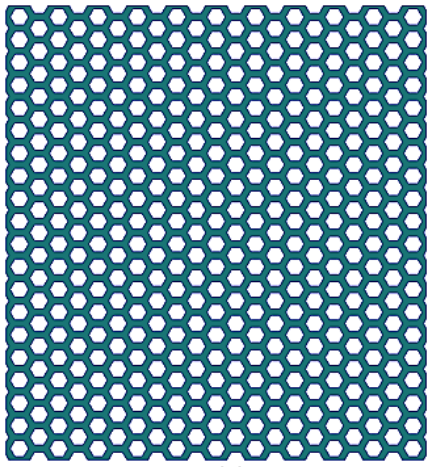

(g)

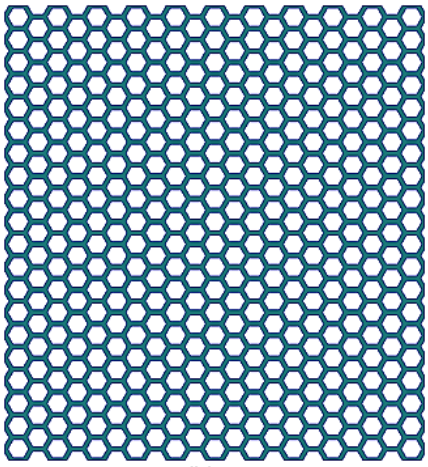

(h)

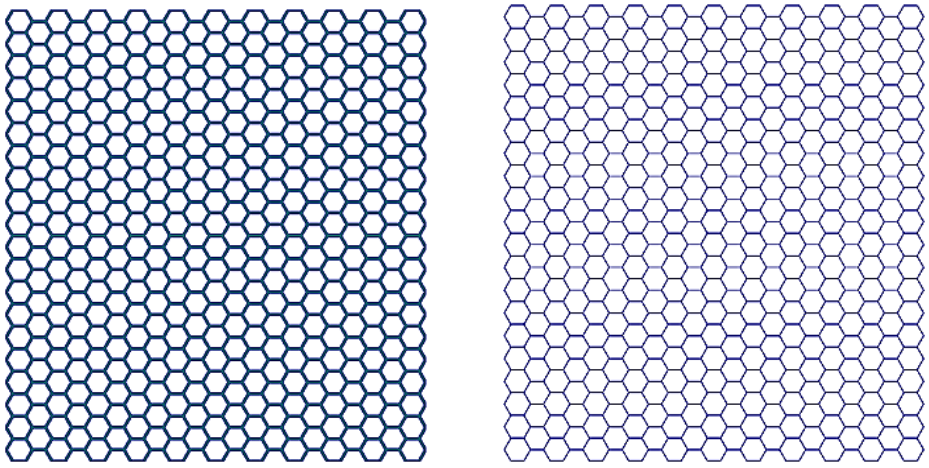

(i) (j)

Figure 2-10 Varying relative density of honeycomb with regularity δ = 1.0. (a) $\bar{\rho}$ = 0.991 (b) $\bar{\rho}$ = 0.963 (c) $\bar{\rho}$ = 0.916 (d) $\bar{\rho}$ = 0.850 (e) $\bar{\rho}$ = 0.766 (f) $\bar{\rho}$ = 0.662 (g) $\bar{\rho}$ =0.538 (h) $\bar{\rho}$ = 0.395 (i) $\bar{\rho}$ = 0.231 (j) $\bar{\rho}$ = 0.048

The cell wall thicknesses previously calculated for the regular honeycomb are applied to the irregular honeycomb. The corresponding relative densities for the irregular honeycomb are tabulated in Table 2-2. Similarly, the irregular honeycomb geometries are presented in Figure 2-11.

Table 2-2 Relative densities for honeycomb with regularity δ = 0.75

Cell Wall Thickness (t_w)	Relative Density ($\bar{\rho}$) for δ = 0.75
37.9	0.996
33.8	0.981
29.7	0.942
25.6	0.879
21.5	0.791
17.4	0.686
13.3	0.554
9.2	0.405
5.1	0.239
1	0.049

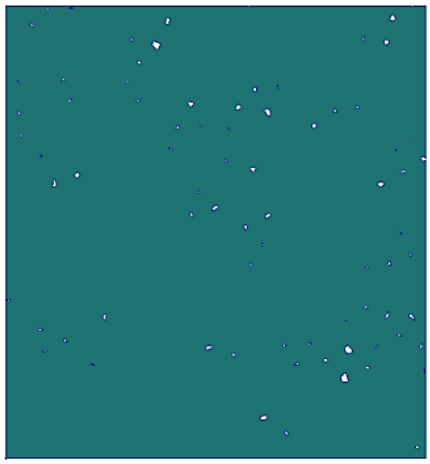

(a)

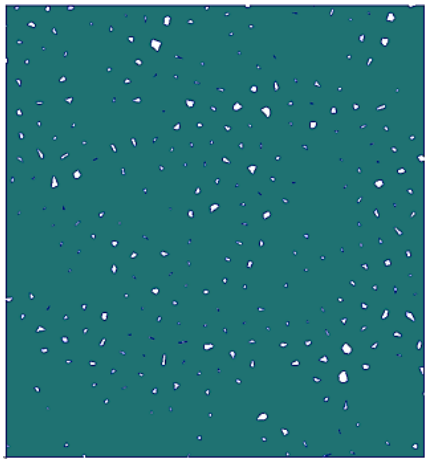

(b)

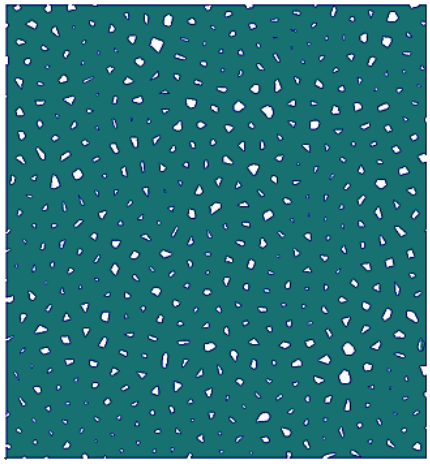

(c)

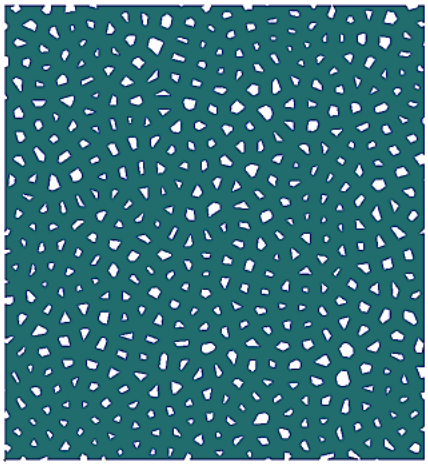

(d)

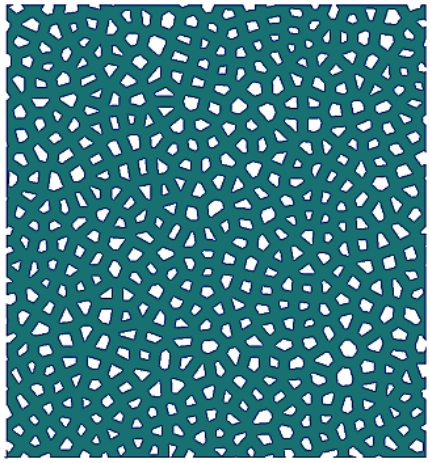

(e)

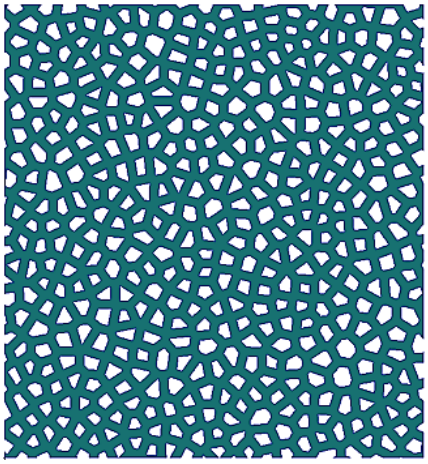

(f)

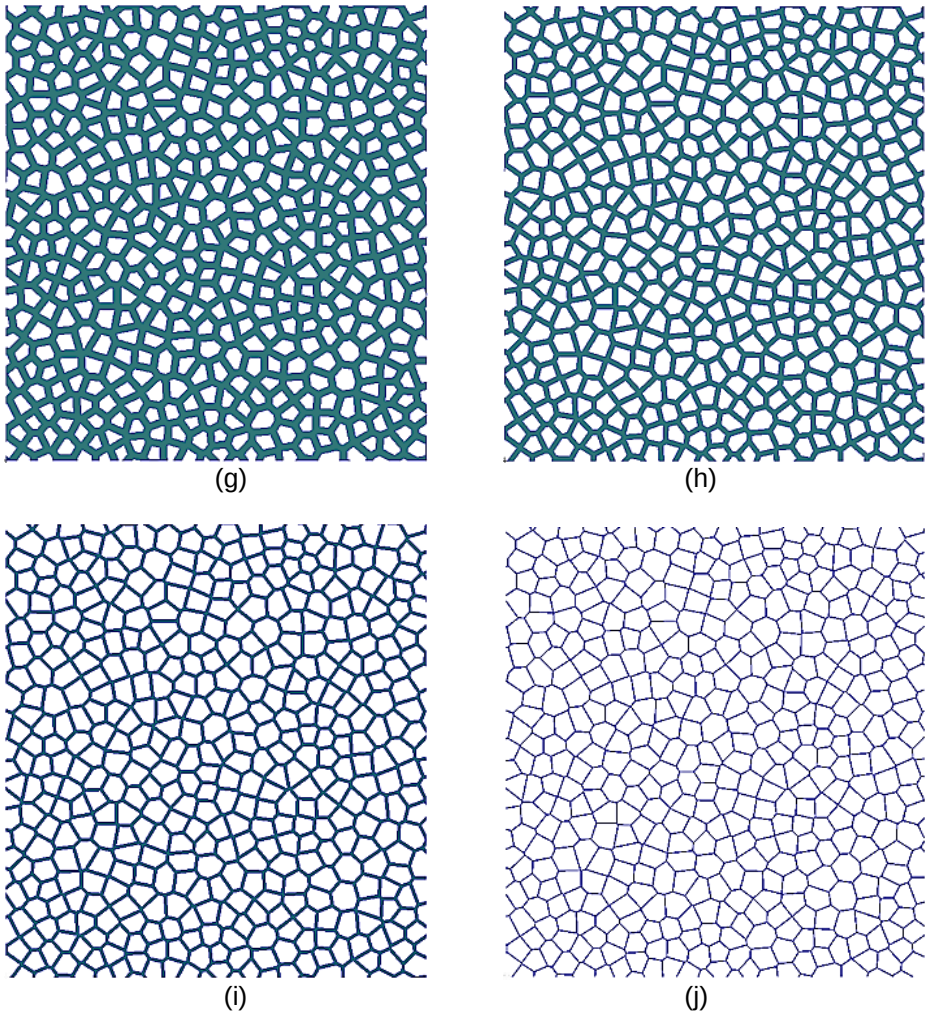

Figure 2-11 Varying relative density of a honeycomb with regularity δ = 0.75.
(a) $\bar{\rho}$ = 0.996 (b) $\bar{\rho}$ = 0.981 (c) $\bar{\rho}$ = 0.942 (d) $\bar{\rho}$ = 0.879 (e) $\bar{\rho}$ = 0.791 (f) $\bar{\rho}$ = 0.686
(g) $\bar{\rho}$ =0.554 (h) $\bar{\rho}$ = 0.405 (i) $\bar{\rho}$ = 0.239 (j) $\bar{\rho}$ = 0.049

2.3 Finite Element Modeling

2.3.1 Isotropic Microstructural Properties

The geometries are then imported from Siemens NX™ to MSC Patran via a Parasolid Model Part file (*.x_t). Each specimen is finely meshed via a combination of quadrilateral, CQUAD4, and triangular, CTRIA3, isoparametric plane strain elements.

Triangular elements are not ideal because their strain matrix is constant. This makes them excessively stiff and less accurate than quadrilateral elements [33]. While quadrilateral elements are preferred, their sole use is infeasible. The cell walls are discretized with at least two rows of quadrilateral elements. However, the complex geometry requires the implementation of triangular elements at the cell wall junctions, as shown in Figure 2-12 for the irregular honeycomb with relative density of 0.049.

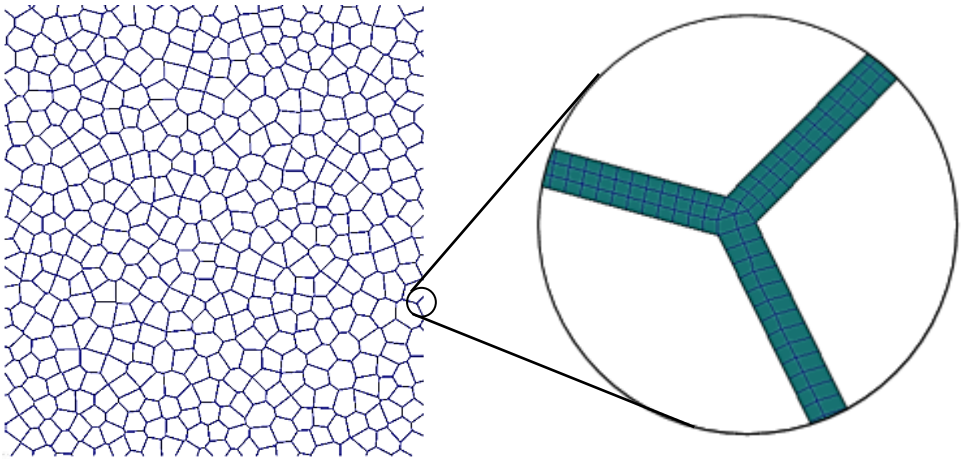

Figure 2-12 Cell walls discretized with 2D plane strain elements

The use of triangular elements is extremely small. For the honeycomb depicted in Figure 2-12, triangular elements constitute less than 0.05% of the elements. Therefore, their use has negligible impact on the overall model stiffness.

The PSHELL property entry is used to define the properties of the aforementioned elements [33]. The specimens are modeled using the properties of 7075-T6 Bare Aluminum which are described in Table 2-3.

Table 2-3 Material properties of 7075-T6 Bare Aluminum [1]

Elastic Modulus, E_s (GPa)	Shear Modulus, G_s (GPa)	Poisson's Ratio, ν_s	Density, ρ_s (kg / m^3)
71.02	26.89	0.33	2800

The loads and boundary conditions required to investigate the effective mechanical properties of the geometries presented in Figure 2-10 and Figure 2-11 are shown in Figure 2-13 through Figure 2-15. The loads and boundary conditions are shown for the fully developed hexagonal honeycomb; however, the model setups are applicable to all geometries. Figure 2-13 shows the model setup for determining the elastic modulus E_x^* and Possion's ratio ν_{xy}^* for loading in the x-direction.

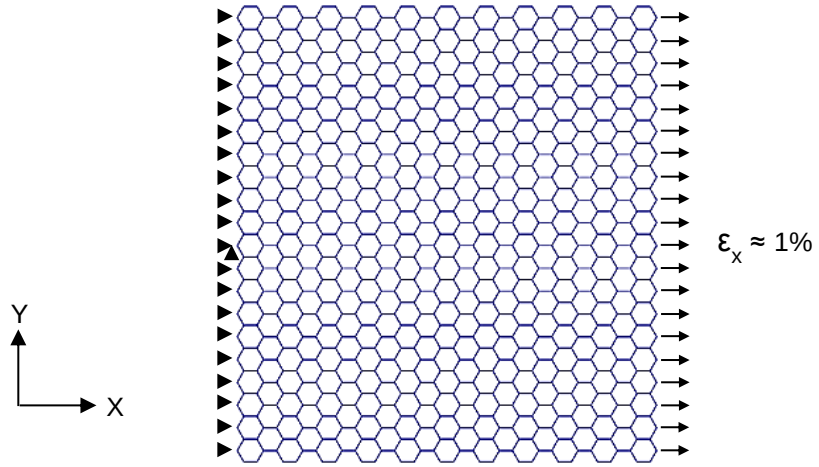

Figure 2-13 Model setup for calculation of elastic modulus and Poisson's ratio for x-direction loading

As shown in the figure, a displacement, corresponding to a strain ε of 1%, is applied in the x-direction to the nodes along the right hand side of the specimen (denoted by →). The nodes along the left hand side are constrained in x-direction (denoted by ►). A single node on the left hand side that is vertically centered is constrained in the y-direction (denoted by ▲). Lastly, all nodes along the perimeter of the specimen are constrained in the z-direction or out-of-plane direction (not shown). Thus, the model is fully constrained. The applied displacement generates reaction forces on the nodes constrained in the x-direction. These reaction forces are summed and then divided by the cross-sectional area to yield the tensile stress induced on the specimen. The stress is

then divided by the applied strain to yield the elastic modulus of the specimen. As the specimen expands in the longitudinal direction (direction of applied loading), it contracts in the lateral direction. The Poisson's ratio is then calculated by taking the negative ratio of lateral strain to longitudinal strain. For Figure 2-13, the Poisson's ratio is calculated for each node along the top edge of the specimen. The Poisson's ratios are then averaged to obtain a final value.

The same methodology is used to calculate the elastic modulus E_y^* and Possion's ratio ν_{yx}^* for loading in the y-direction, as shown in Figure 2-14.

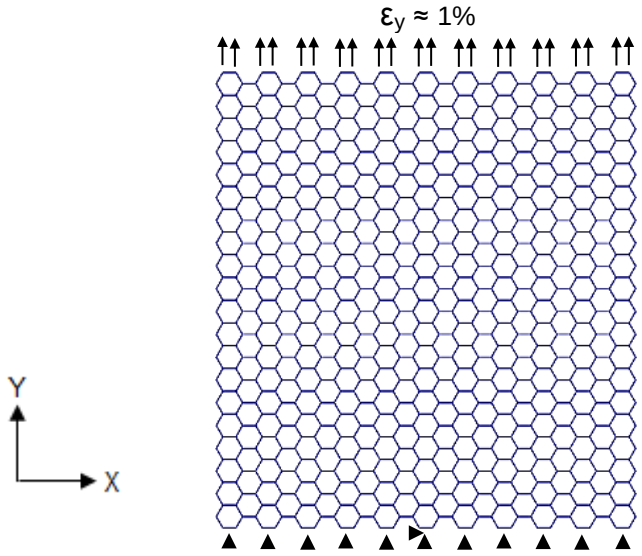

Figure 2-14 Model setup for calculation of elastic modulus and Poisson's ratio for y-direction loading

Figure 2-15 demonstrates the model setup for calculating the shear modulus G_{xy}^* for loading in the x-direction. As shown in the figure, a displacement, corresponding to a strain γ of 1%, is applied in the x-direction to the nodes along the top of the specimen (denoted by $\rightarrow$). The nodes along the bottom are constrained in x-direction (denoted by ►). Lastly, all nodes along the perimeter of the specimen are constrained in the y-direction and the z-direction (not shown). Thus, the model is fully constrained. The

applied displacement generates reaction forces on the nodes constrained in the x-direction. These reaction forces are summed and then divided by the cross-sectional area to yield the shear stress induced on the specimen. The stress is then divided by the applied strain to yield the shear modulus of the specimen.

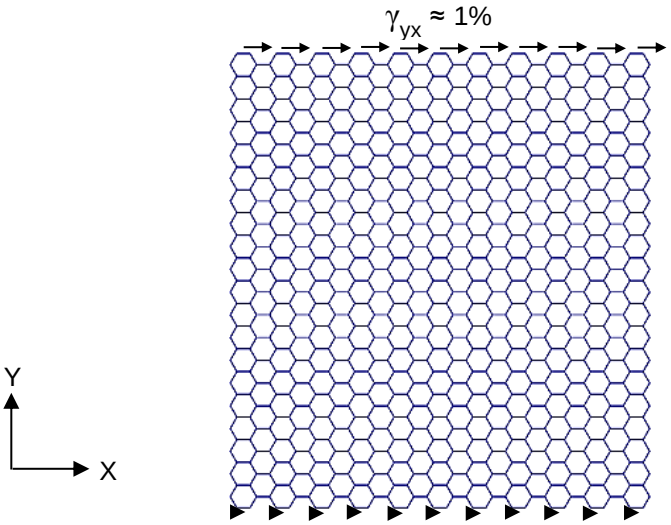

Figure 2-15 Model setup for calculation of shear modulus for x-direction loading

The same methodology is used to calculate the shear modulus G_{yx}^{*} for loading in the y-direction, as shown in Figure 2-16.

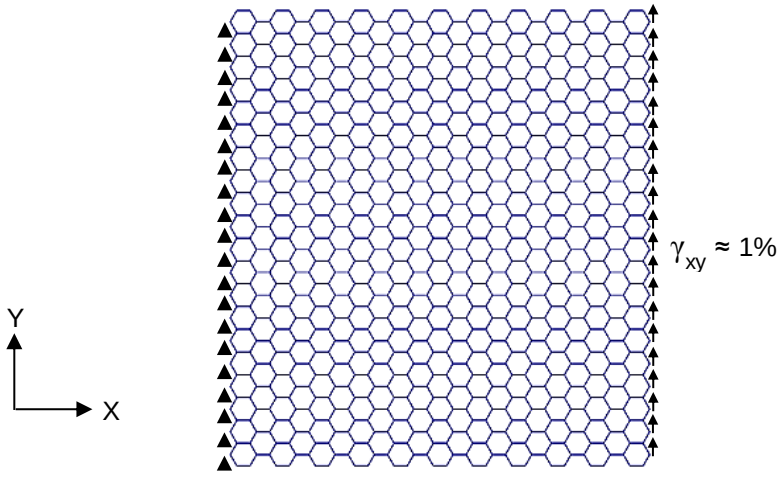

Figure 2-16 Model setup for calculation of shear modulus for y-direction loading

The relative elastic modulus $\bar{E}$ is calculated by dividing the elastic modulus of the specimen, E_x^* or E_y^*, by the elastic modulus of the of the base material E_s. Similarly, the relative shear modulus $\bar{G}$ is calculated by dividing the shear modulus of the specimen, G_{xy}^* or G_{yx}^*, by the elastic modulus of the of the base material E_s.

2.3.2 Anisotropic Microstructural Properties

The anisotropic models are created from the isotropic models and maintain identical geometry, elements, nodes, loads, and boundary conditions. The only difference is the material property of the solid. A local coordinate system is constructed for each ligament such that the x-axis corresponds to the longitudinal direction and the y-axis corresponds to the lateral direction. Each element property is applied in the local coordinate system of the ligament it belongs to. An example of the local coordinate systems is illustrated in Figure 2-17.

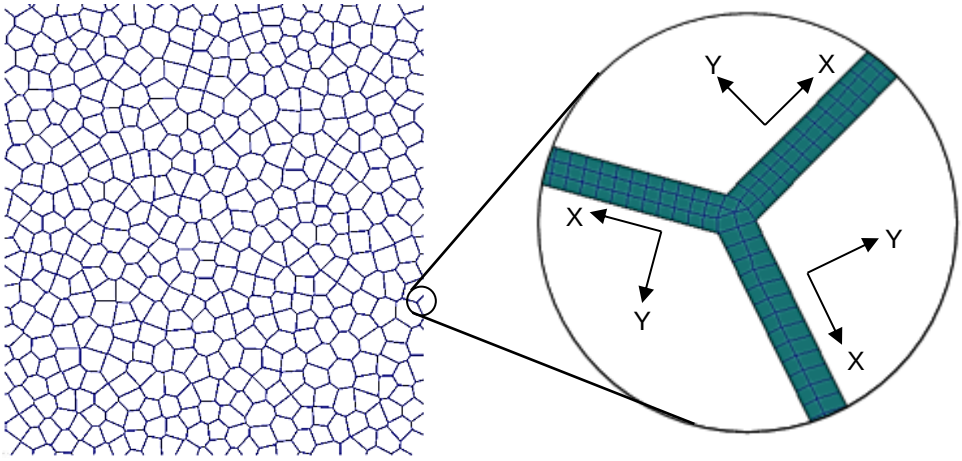

Figure 2-17 Local coordinate system definition

The elements making up the junction do not belong to a specific ligament and therefore, are not assigned anisotropic properties. Instead, they retain the isotropic

properties used for the isotropic models. For the hexagonal honeycombs, the ligaments are oriented at 0 degrees, 60 degrees, and 120 degrees from the horizontal axis. Thus, only three coordinate systems are required. For the irregular honeycombs, each ligament is at a unique angle above the horizontal axis and requires its own unique local coordinate system. This quickly adds up to over 1,300 coordinate systems. The time consuming task of creating the coordinate systems and applying the element properties is accomplished in Microsoft Excel via several VBA Macros. The geometric, elemental, and nodal data contained in the MSC Patran input file (*.bdf) is extracted and imported into Excel. The VBA Macros create a coordinate system for each ligament, locate the elements belonging to a respective ligament, apply the appropriate elemental property, and then create a new .bdf input file for MSC Patran. The coordinate systems are applied using the CORD2R entry and the anisotropic properties are applied using the MAT8 entry [33].

Many cellular materials in nature exhibit significant anisotropic properties. For example, cork has an elastic modulus of 13 MN/m^2 in the axial direction and 20 MN/m^2 in the radial direction [19]. Similarly, wood is significantly stronger in the axial direction when compared to the radial direction. For instance, balsa wood has an elastic modulus of 6 GPa in the axial direction and 0.3 GPa in the radial direction [39]. Therefore, the finite element models are given properties that capture significant anisotropy. Two separate material property scenarios are considered. The first case defines properties such that stiffness in the elemental x-direction is greater than stiffness in the elemental y-direction and the second case vice versa. The properties used for the anisotropic models are defined in Table 2-4.

Table 2-4 Anisotropic material properties

	Elastic Modulus, E_{sx} (GPa)	Elastic Modulus, E_{sy} (GPa)	Shear Modulus, G_s (GPa)	Poisson's Ratio, ν_{sxy}	Poisson's Ratio, ν_{syx}	Density, ρ_s (kg / m^3)
Case 1	71.02	35.51	26.89	0.33	0.165	2800
Case 2	35.51	71.02	26.89	0.165	0.33	2800

The subscript *s* indicates that the property pertains to the solid material to avoid confusion between the global mechanical properties and the properties of the solid material. For Case 1, the elastic modulus in the longitudinal direction, E_{sx}, the shear modulus, G_s, the Poisson's ratio, v_{sxy}, and the density, ρ_s, are the same as the isotropic material properties in Table 2-3. The elastic modulus in lateral direction, E_{sy}, is chosen to be half of the elastic modulus in the longitudinal direction, E_{sx}. The Poisson's ratio, v_{syx}, is not an input in the MAT8 property entry. Instead, MSC Patran calculates v_{syx} internally using the following relationship [33],

$$E_{sx}\nu_{syx} = E_{sy}\nu_{sxy} \tag{10}$$

For Case 2, the elastic modulus in the lateral direction, E_{sy}, the shear modulus, G_s, the Poisson's ratio, v_{syx}, and the density, ρ_s, are the same as the isotropic material properties in Table 2-3. The elastic modulus in longitudinal direction, E_{sx}, is chosen to be half of the elastic modulus in the lateral direction, E_{sx}. The two aforementioned cases capture the influence of microstructural anisotropy for a dominant stiffness in either the x or y-direction.

For the anisotropic models, the effective elastic and shear moduli are calculated by dividing the elastic and shear moduli of the specimen by the elastic modulus of the isotropic base material described in Table 2-3.

Chapter 3

Isotropic Analysis

3.1 Theoretical Analysis of Hexagonal Honeycombs

Using Timoshenko beam theory, Gibson et al. [19, 20] derived formulae that accurately describe the five in-plane mechanical properties (E_x, E_y, G_{xy}, v_{xy}, and v_{yx}) of hexagonal honeycombs (δ = 1). Their original derivation utilized Euler-Bernoulli beam theory which solely accounted for cell wall bending and ignored axial and shear contributions. Through experimental tests, they substantiated their bending only formulae for low relative densities [20]. While cell wall bending is the primary source of deformation, they point out that the contribution of axial and shear deformation significantly increases as the relative density increases. As acknowledged by Silva, Hayes, and Gibson [38], axial and shear deformation constitute approximately 10% of the total deformation for a relative density of 0.15. Therefore, Gibson and Ashby [19] derive a new set of equations, using Timoshenko beam theory, that account for the contributions of axial and shear deformations, which are presented below.

$$\bar{\rho} = \frac{\rho^*}{\rho_s} = \left(\frac{t_w}{l}\right) \frac{(h/l)+2}{2\cos\theta\left((h/l)+\sin\theta\right)} \tag{11}$$

$$\bar{E}_y = \frac{E_y^*}{E_s} = \frac{(t_w/l)^3 \cos\theta}{(h/l+\sin\theta)\sin^2\theta} \; \frac{1}{1+(2.4+1.5\nu_s+\cot^2\theta)(t_w/l)^2} \tag{12}$$

$$\bar{E}_x = \frac{E_x^*}{E_s} = \frac{(t_w/l)^3(h/l+\sin\theta)}{\cos^3\theta} \; \frac{1}{1+\left(2.4+1.5\nu_s+\tan^2\theta+\frac{2(h/l)}{\cos^2\theta}\right)\left(\frac{t_w}{l}\right)^2} \tag{13}$$

$$\bar{G}_{xy} = \frac{G_{xy}^*}{E_s} = \frac{(t_w/l)^3(h/l+\sin\theta)}{(h/l)^2\cos\theta\left[1+2(h/l)+(t_w/l)^2\right]} \times \frac{1}{\left[\left(\frac{2.4+1.5\nu_s}{h/l}\right)(2+h/l+\sin\theta)+\left(\frac{h/l+\sin\theta}{(h/l)^2}\right)(h/l+\sin\theta)\tan^2\theta+\sin\theta\right]} \tag{14}$$

$$\nu_{yx}^{*} = \frac{\cos^2\theta}{(h/l+\sin\theta)\,sin\,\theta}\ \frac{1+(1.4+1.5\nu_s)(t_w/l)^2}{1+(2.4+1.5\nu_s+\cot^2\theta)(t_w/l)^2} \tag{15}$$

$$\nu_{xy}^{*} = \frac{(h/l+\sin\theta)\,sin\,\theta}{\cos^2\theta}\ \frac{1+(1.4+1.5\nu_s)(t_w/l)^2}{1+\left(2.4+1.5\nu_s+\tan^2\theta+\frac{2(h/l)}{\cos^2\theta}\right)\left(\frac{t_w}{l}\right)^2} \tag{16}$$

ρ^*, E^*, G^*, and ν^* are the density, Young's Modulus, Shear Modulus, and Poisson's ratio of the cellular structure and ρ_s, E_s, G_s, and ν_s are the density and moduli of the solid material from which it is made (reference Table 2-3 for material properties). The variables h, l, t_w, and θ are illustrated in Figure 3-1.

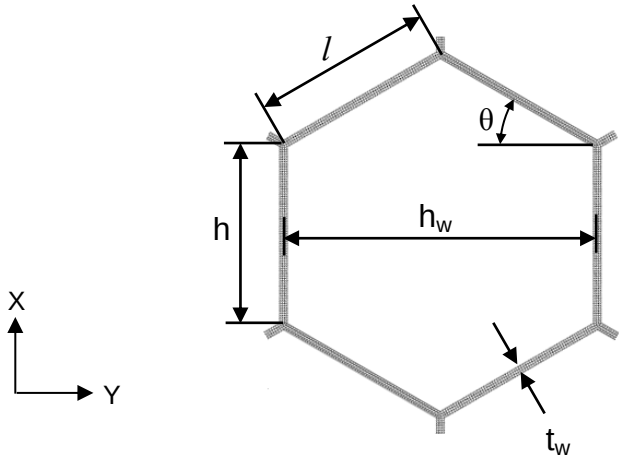

Figure 3-1 Hexagonal unit cell

The cell wall thickness is denoted by t_w, cell wall angle by θ, and cell wall length by h and l. For regular hexagonal cells, h and l are equivalent and θ is equal to 30 degrees. As discussed in Section 2.2, h_w is the cell height. As relative density increases, the cell walls thicken and the cell height decreases. Therefore, the cell wall thickness and cell height are the only variables that change with varying relative densities (reference Table 2-1). The aforementioned equations are used to validate the finite element models that have low relative densities and thus, behave as cellular solids.

3.2 Theoretical Analysis of Porous Media

The effective elastic properties of materials containing defects such as voids is a popular topic of interest and has been studied for several decades. Numerous theoretical methods have been developed in an attempt to estimate the properties of these porous media. Hu and colleagues [26] indicate that some of the most prominent micromechanical methods include the Mori-Tanaka method (M-T) [3, 40], the generalized self-consistent method (GSCM) [27], the interaction direct derivative method (IDD) [13, 45], and the composite cylinder model (CCM) [22, 23]. These models were developed to estimate the effective Young's modulus and shear modulus of particle reinforced composites and fiber reinforced composites. However, the theory developed by these models can be applied to the case of a material containing empty voids. The theory and application of these models is a rigorous and labor-intensive process that is beyond the scope of this thesis. Fortunately, Hu applied these methods to a plate containing randomly generated holes [26]. Therefore, the theoretical results obtained by Hu are leveraged and used for comparison. For convenience, a brief discussion of each method is presented in the following paragraphs.

The Mori-Tanaka method (M-T) assumes that the average strain in the inclusion is related to the average strain in the matrix by a fourth order tensor. The approximated fourth order tensor is then used to estimate the effective moduli [3]. One disadvantage of this method is that it assumes that each inclusion is embedded in an infinite matrix. Therefore, this method fails to account for void interaction which leads to erroneous estimates for high void concentrations [45].

The generalized self-consistent method (GSCM) is based on the strain energy equivalence framework proposed by Budiansky [4]. The GSCM improves Budiansky's

method by incorporating the three phase model (void-matrix-composite model) proposed by Christensen and Lo [7]. The three-phase model considers the inclusion as embedded in a finite matrix layer which is then embedded in an infinite effective medium. The advantage of this model is that it is capable of capturing the interaction among inclusions. However, the inclusions are restricted to spherical and cylindrical geometries. Another disadvantage, as noted by Klusemann and Svendsen [29], is the complexity in application due to its implicit structure.

The interaction direct derivative method (IDD) employs the same three-phase model as the GCSM. Unlike the GCSM, the IDD is not restricted to spherical and cylindrical geometries and its application is much simpler due to its explicit structure. The spherical and cylindrical geometric restrictions are circumvented when assuming the void to be an ellipsoid [45]. Additionally, the estimated effective moduli are independent of void size and distribution.

The composite cylinder model (CCM), also known as the composite cylinder assemblage model, estimates the effective properties of a homogeneous and transversely isotropic fiber-reinforced composite [22, 23]. The model considers the composite as the assemblage of parallel cylindrical fibers embedded in a matrix material. When the model is subjected to uniform strains, the effective elastic moduli may be determined from the strain energy by using variation principles [24]. This method is incapable of providing exact solutions and is limited to estimating the upper and lower bounds of the effective properties.

A means of determining the Poisson's Ratio for porous media has been proposed by Day, Snyder, Garboczi, and Thorpe [10]. The aforementioned authors studied the properties of a sheet containing equal sized circular holes where the hole centers are arranged in a hexagonal lattice. Their analysis employed a discretized spring

scheme on a digital image based model. This method allowed them to represent the pixels of an image on a lattice so that the mathematical operations can be carried out on the lattice rather than the continuum. They then construct a spring network connecting each pixel to its nearest neighbors. Their expression for Poisson's ratio is an interpolation of the Milton Proof [10] which derived the Poisson's ratio at a percolation threshold, ρ_c. The percolation threshold is defined as the area fraction when the circular holes touch. Recall equation (2) in Section 2.1.1 which provided the packing density η for the hexagonal lattice arrangement. For the hexagonal arrangement of circular holes, Day and colleagues [10] define the percolation threshold as

$$\rho_c = 1 - \eta = 0.0931 \tag{17}$$

They then express the Poisson's ratio for varying relative densities with the following interpolation formula:

$$\nu^* = \frac{1}{3}\left(1 - \left[\frac{1-\bar{\rho}}{1-\rho_c}\right]^n\right) + [1 + \alpha(\bar{\rho} - \rho_c)]\left[\frac{1-\bar{\rho}}{1-\rho_c}\right]^n \tag{18}$$

where the number of holes n in a unit area is equal to 4 and the adjustable parameter α is equal to 2.5. The adjustable parameter was first introduced by Garboczi [17] in order to optimize the fits between the interpolation formula and his experimental data. The same intent was later adopted by Day et al. [10]. Equation (18) is used to validate the Poisson's ratios obtained from the finite element models.

3.3 Finite Element Analysis Results

The finite element analysis results are shown in Figure 3-2 which plots the relative Young's modulus $\bar{E}$, relative shear modulus $\bar{G}$, and Poisson's ratio ν^* versus relative density $\bar{\rho}$. The black data represents the regular honeycomb (δ = 1) and the red data represents the irregular honeycomb (δ = 0.75). The solid lines represent $\bar{E}_x$, $\bar{G}_{xy}$,

and ν_{xy}^* while the dashed lines represent $\bar{E}_y$, $\bar{G}_{yx}$, and ν_{yx}^*. Additionally, all of the results are tabulated in Appendix B.

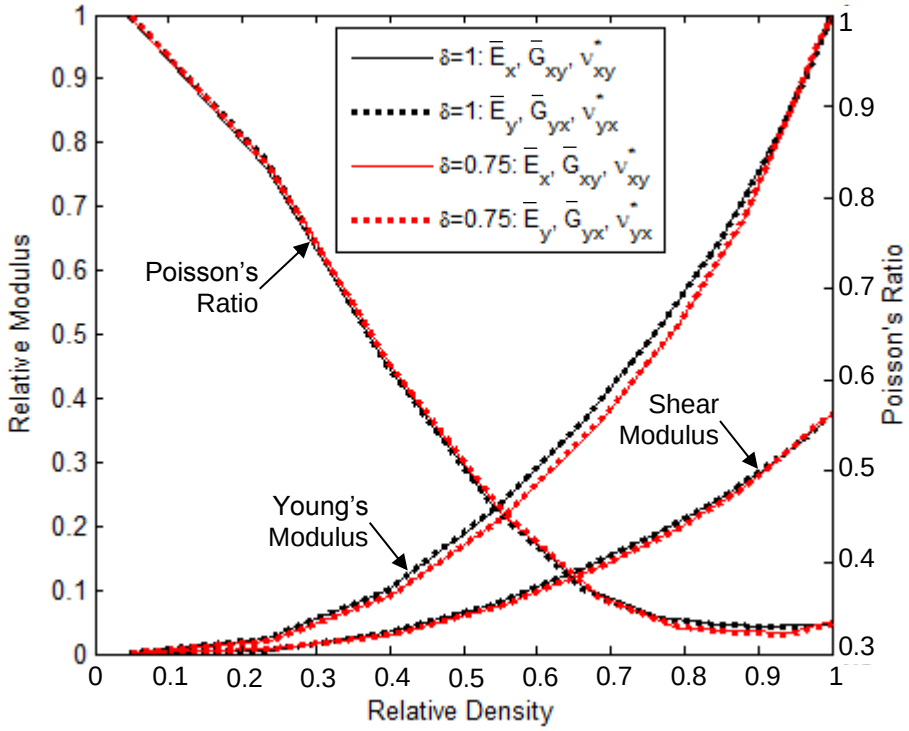

Figure 3-2 Relative moduli and Poisson's ratio vs relative density

For both the regular and irregular arrangements, loading direction has minimal impact on the global mechanical properties. While the impact is minimal, lower relative densities exhibited the largest variations in properties. For the regular arrangement at a relative density of 0.048, $\bar{E}_x$ and $\bar{E}_y$ vary by 2.0%, $\bar{G}_{xy}$ and $\bar{G}_{yx}$ vary by 2.0%, and ν_{xy}^* and ν_{yx}^* vary by 1%. For larger relative densities, the variations are below 1%. Per the theoretical analysis put forth by Gibson and Ashby [19], the material properties of isotropic hexagonal honeycombs are not dependent on direction (i.e. $\bar{E}_x = \bar{E}_y$, $\bar{G}_{xy} = \bar{G}_{yx}$, and $\nu_{xy}^* = \nu_{yx}^*$). The aforementioned variances are small and are considered in agreement with their theoretical analysis. Additionally, Vajjhala's [42] finite element analysis of a

hexagonal honeycomb with relative density of 0.15 resulted in slightly over a 1% difference in $\bar{E}_x$ and $\bar{E}_y$. The same trend in property differences was found for the irregular arrangement, as well. For the irregular arrangement at a relative density of 0.049, $\bar{E}_x$ and $\bar{E}_y$ vary by 1.5%, $\bar{G}_{xy}$ and $\bar{G}_{yx}$ vary by 1.5%, and ν_{xy}^* and ν_{yx}^* vary by 1%. Similarly, for larger relative densities, the variations are below 1%. These property differences at low relative densities are expected. For twenty irregular honeycombs with relative density of 0.15 and regularity 0.7, Silva and colleagues [38] report differences in $\bar{E}_x$ and $\bar{E}_y$ up to 12% with an average of only 1%. They also report differences in ν_{xy}^* and ν_{yx}^* up to 19% with an average of only 1%. Additionally, Vajjhala's [42] finite element analysis of an irregular honeycomb with relative density of 0.15 resulted in a 7% variance in $\bar{E}_x$ and $\bar{E}_y$ (regularity not clearly defined, speculated to be 0.7).

It is interesting to compare the properties of the regular arrangement to the irregular arrangement. The relative Young's moduli of both arrangements vary by a few percent for most ranges of relative densities. The greatest variances occur for low relative densities where the structures exhibit cellular behavior. At a relative density of 0.049, the irregular arrangement is approximately 6.5% stiffer than the regular arrangement. Similarly, the shear moduli vary by a few percent for most ranges of relative densities with the greatest variances occurring for low relative densities. At a relative density of 0.049, the irregular arrangement is roughly 13% higher than the regular arrangement. Interestingly, the Poisson's ratio consistently differs by several percent for nearly all ranges of relative density. At a relative density of 0.049, the irregular arrangement is about 3.5% lower than the regular arrangement. These results are in close agreement with the twenty irregular models analyzed by Silva and colleagues [38]. They found that the relative Young's modulus varied up to 26% with an average increase of 6%, the

relative shear modulus varied up to 28% with an average increase of 11%, and the Poisson's ratio varied up to 9% with an average decrease of 1% [38].

Each of the properties previously discussed are isolated and compared to the theoretical methods presented in Sections 3.1 and 3.2. The relative Young's moduli are shown in Figure 3-3, the relative shear moduli are shown in Figure 3-6, and the Poisson's ratios are shown in Figure 3-7.

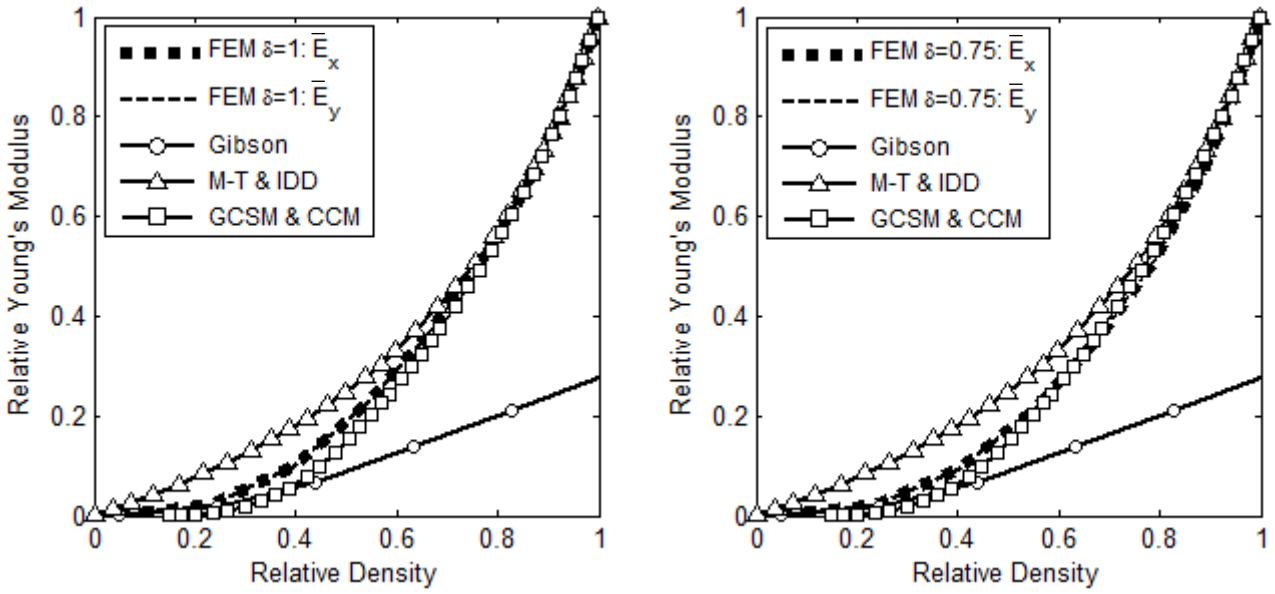

Figure 3-3 Relative Young's modulus vs relative density with regularity (a) δ = 1 and (b) δ = 0.75

Figure 3-3(a) and 3-3(b) plot the relative Young's modulus against relative density for the regular and irregular arrangements. It is apparent from the above figures that the generalized self-consistent method (GSCM) and the composite cylinder model (CCM) yield reasonable trends for the full range of relative densities while the Mori-Tanaka method (M-T) and the interaction direct derivative method (IDD) only provide meaningful results at high relative densities. Unsurprisingly, Gibson's formulation produces meaningful results at low relative densities. For large relative densities of the

regular arrangement in Figure 3-3(a), the M-T and IDD models predict relative Young's moduli that are within a few percent of the FEM results. As the relative density decreases, the difference between the FEM and the M-T and IDD models increases; achieving a 10% difference at a relative density of 0.65. As the relative density continues to decrease, the models drastically over predict the relative Young's modulus. This deviation is due to the fact that the M-T and IDD models do not take into account void distribution and interaction and thus, lose their usefulness. The same phenomenon can be said for the irregular arrangement in Figure 3-3(b); except that the 10% deviation occurs for a relative density of about 0.75. Similar to the M-T and IDD models, the GSCM and CCM models produce accurate results at larger relative densities. These models achieve a 10% deviation at a relative density of about 0.6 for the regular arrangement and roughly 0.5 for the irregular arrangement. While the deviation is not as drastic as the M-T and IDD models, it is nonetheless significant with deviations upwards of 200% for low relative densities. The GSCM and CCM models produce better results than the M-T and IDD models since they are equipped to handle void interaction. However, it is noted that their application is for circular voids and not for polygonal voids as in our case. It is believed that our unique void geometry may contribute to the large deviations at low relative densities. It is worth noting that these results corroborate the work of Hu et al. [26] who obtained similar results for a plate containing non-overlapping circular holes. Their analysis concludes that the GSCM and CCM schemes provide reasonable results for the entire spectrum of relative densities while the M-T and IDD schemes severely under predict the hole interaction and are only applicable to high relative densities.

Gibson et al. [19, 37, 38] has consistently maintained that their theoretical formulations (discussed in Section 3.1) are applicable to isotropic hexagonal honeycombs with relative densities up to 0.3. At this relative density, Gibson's formulation

under predicts the FEM results for the regular arrangement by roughly 50%. For the irregular arrangement, the under prediction is approximately 45%. It is hypothesized that these large differences are attributed to the modeling technique employed. Recall that the honeycomb structures are modeled as meshed two-dimensional plates (reference Section 2.3). As the ligament width t_w increases, the ligament length *l* decreases. This is dissimilar to Gibson's formulation which measures the ligament length from the center points of the ligament intersections. Each scenario is depicted in Figure 3-4.

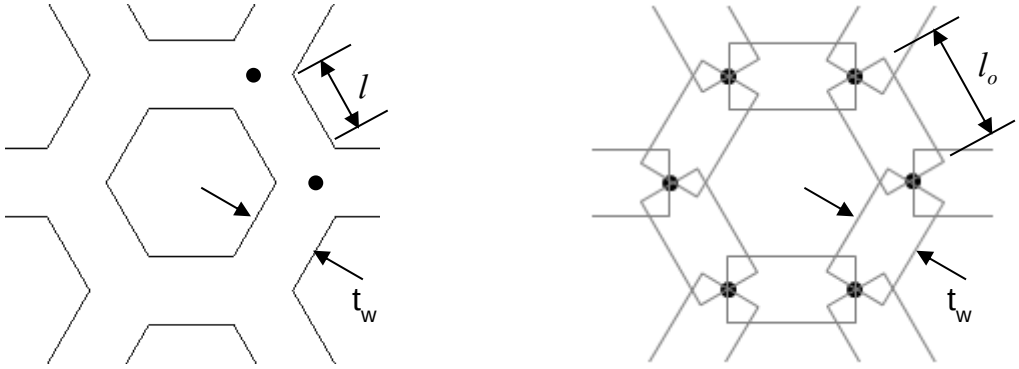

(a) (b)

Figure 3-4 Analysis dimensions (a) FEM, (b) Gibson's formulation

As can be seen, the ligament length remains constant for Gibson's analysis while it shrinks in the finite element analysis. Therefore, Gibson's analysis analyzes beams that are longer than what is actually present. The reduction in ligament length increases the ligaments stiffness which is not accounted for in the analytical approach. This additional stiffness can be accounted for by adapting Gibson's measurement for ligament length. Using simple trigonometry, the new ligament length in Figure 3-4(a) is calculated.

$$l = l_o - t_w(\cos 30° - 0.5 \tan 30°) \tag{19}$$

Gibson's prediction for the relative Young's modulus is recalculated using the above equation. Figure 3-5 recreates Figure 3-3 using the updated ligament length. The data resulting from the modified ligament length is represented by the red line.

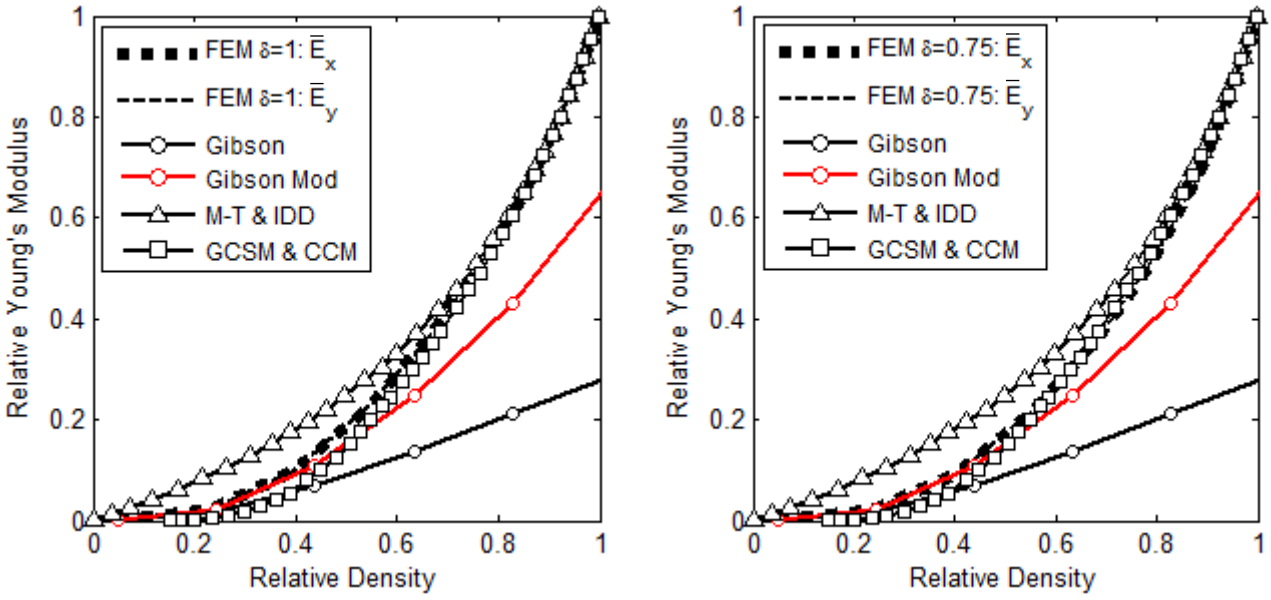

Figure 3-5 Updated Relative Young's modulus vs relative density with regularity (a) δ = 1 and (b) δ = 0.75

From inspection of Figure 3-5, it is obvious that the updated Gibson formulation yields much more accurate results. Recall that at a relative density of 0.3, Gibson's formulation originally under predicted the FEM results for the regular arrangement by roughly 50% and the irregular arrangement by about 45%. Using the updated ligament length, Gibson's formulation now differs from the FEM by 4% for the regular arrangement and 3% for the irregular arrangement. This is a significant improvement; thus, confirming the hypothesis regarding ligament length. It can be argued that Gibson's equations return acceptable results at higher relative densities. It is at a relative density of just over 0.4 that the regular arrangement produces a 10% difference. Similarly, it is at a relative density of 0.55 that the irregular arrangement produces a 10% difference. As relative density increases, the percent difference climbs to over 50%.

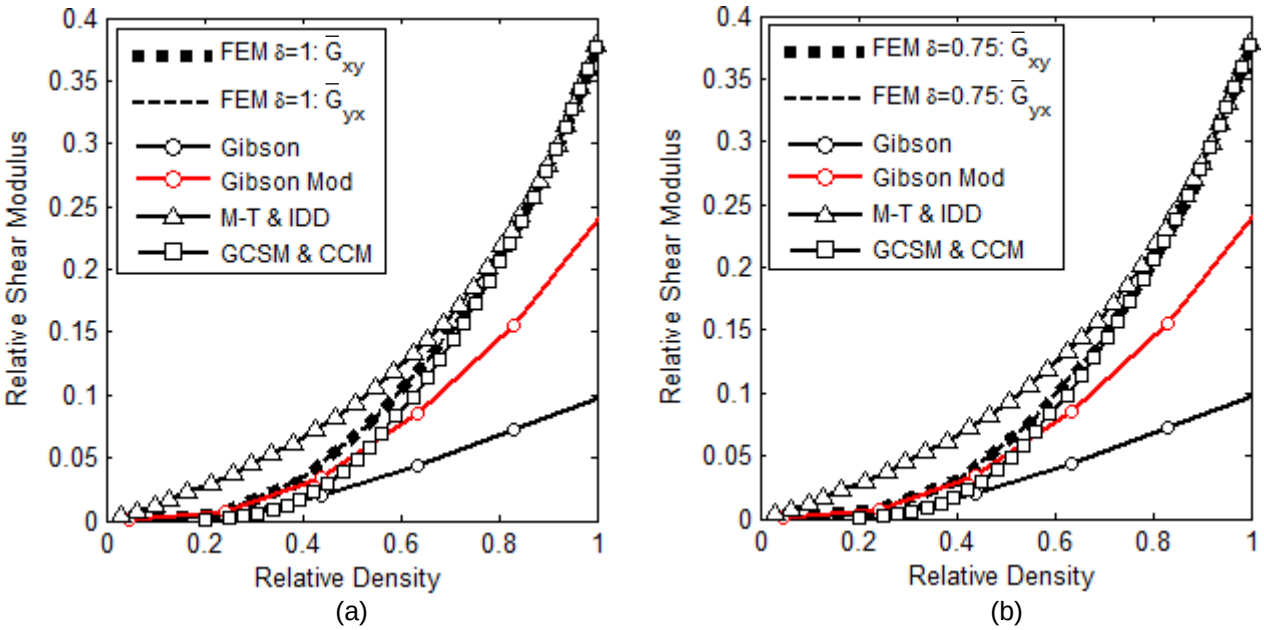

Figure 3-6 Relative shear modulus vs relative density with regularity (a) δ = 1 and (b) δ = 0.75

Figure 3-6(a) and 3-6(b) plot the relative shear modulus against relative density for the regular and irregular arrangements. The same phenomenon witnessed in Figure 3-3 is observed in the relative shear modulus plots. Namely, the M-T and IDD schemes provide accurate results at high relative densities and drastically overestimate the relative shear modulus at low to mid relative densities while the GSCM and CCM schemes produce reasonable trends for the full range of relative densities. More specifically, the M-T and IDD methods differ from the regular honeycomb FEM results by 10% at a relative density of 0.65 and differ from the Voronoi honeycomb FEM results by 10% at a relative density of about 0.7. Below the aforementioned relative densities, the variations drastically increase. Similarly, the GSCM and CCM methods produce accurate results for higher relative densities. When compared to the FEM results, these models achieve a 10% difference at a relative density of 0.65 for the regular arrangement and 0.6 for the irregular arrangement. The discussion for the relative Young's modulus in

Figure 3-3 is also applicable here. Specifically, that the GSCM and CCM schemes produce better results than the M-T and IDD models since they are equipped to handle void interaction. Additionally, these results corroborate the work of Hu et al. [26] who obtained similar results of a plate containing non-overlapping circular holes.

The modified Gibson formulation achieves accurate results for low relative densities. Recall that Gibson's equations are applicable for relative densities up to 0.3 [19, 37, 38]. At this relative density, the modified Gibson equation under predicts the FEM results by roughly 5% for the regular arrangement and by roughly 4% for the irregular arrangement. For comparison, the unmodified Gibson equation produces differences of about 60% for both arrangements. It is obvious from Figure 3-6 that the modified Gibson equation is applicable to relative densities beyond 0.3. For the regular arrangement, a 10% difference occurs at a relative density of just under 0.4 while for the irregular arrangement, the same percent difference occurs at a 0.5 relative density.

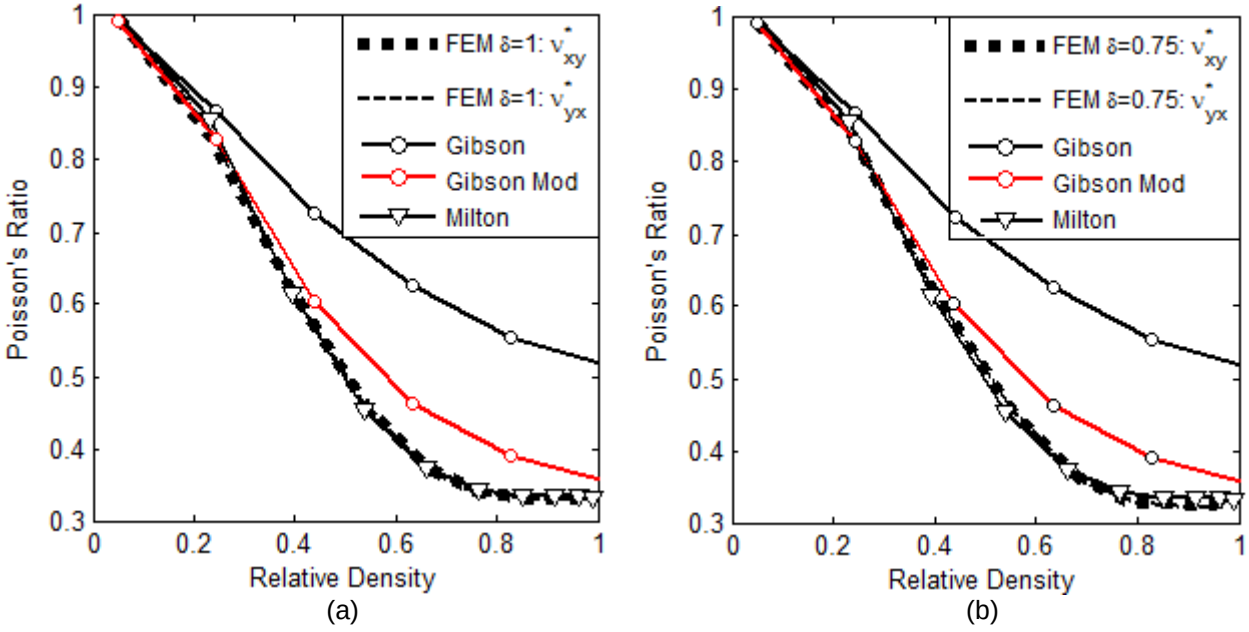

Figure 3-7 Poisson's ratio vs relative density with regularity (a) δ = 1 and (b) δ = 0.75

Figure 3-7(a) and 3-7(b) plot the Poisson's ratio against relative density for the regular and irregular arrangements. With outstanding accuracy, the Milton Proof (reference equation (18) in Section 3.2) predicts the Poisson's ratio of both the arrangements for the full range of relative densities. At most, the Milton Proof differs from the FEM results by 3% for the regular arrangement and 4% for the irregular arrangement. In addition to being independent of void geometry [10], the success of the Milton Proof is attributed to the adjustable parameter α. The adjustable parameter is used to optimize the fits between equation (18) and the FEM results. The downside to this method is that the analyst needs to have experimental data to substantiate the selection of the adjustable parameter. This dilemma can be circumvented by constructing a library of adjustable parameters corresponding to specific hole arrangements (e.g. hexagonal, square, triangular, etc.). For the regular and irregular arrangements analyzed herein, an adjustable parameter of 2.5 provides sufficiently accurate results.

The modified Gibson formulations achieve accurate results for low relative densities. At a relative density of 0.3, the modified Gibson equation over predicts the FEM results by 4% for the regular arrangement and by 3% for the irregular arrangement. The modified Gibson formulation provides the same level of accuracy as the Milton Proof for relative densities below 0.3. For higher relative densities, the modified Gibson equation differs from the FEM results by over 20%. For comparison, the unmodified Gibson equation at a relative density of 0.3 results in a 15% difference for the regular arrangement and 10% difference for the irregular arrangement.

Now that the FEM results have thoroughly been discussed, it is worth revisiting the dilemma concerning the modeling technique and ligament length. Referring back to Figure 3-4(b), Gibson measures the ligament length from the center points of the ligament intersections which remains constant regardless of relative density. It was

proven that this erroneously predicts the global mechanical properties. Throughout the relevant literature [6, 37, 38, 46, 47], researchers model their honeycomb structures with beam elements due to the ease and simplicity. Consequently, it is believed that this erroneous prediction has largely gone unnoticed. In order to understand the implications of these different modeling techniques, the regular honeycomb specimens (reference Figure 2-10) are remodeled using simple beam elements known as CBEAM elements [33]. The CBEAM elements use the PBEAM property entry which implements Timoshenko beam theory; thus, the shear deformations are accounted for. The elements retain the same material properties that are listed in Table 2-3.

Figure 3-8 plots the effective mechanical properties obtained from the quadrilateral isoparametric plane strain elements and the simple beam elements along with the predictions from the modified and unmodified Gibson equations. Since Gibson et al. [19, 37, 38] maintains that their formulations are applicable up to relative densities of 0.3, this portion of Figure 3-8(a), (c), and (e) is magnified in Figure 3-8(b), (d), and (f).

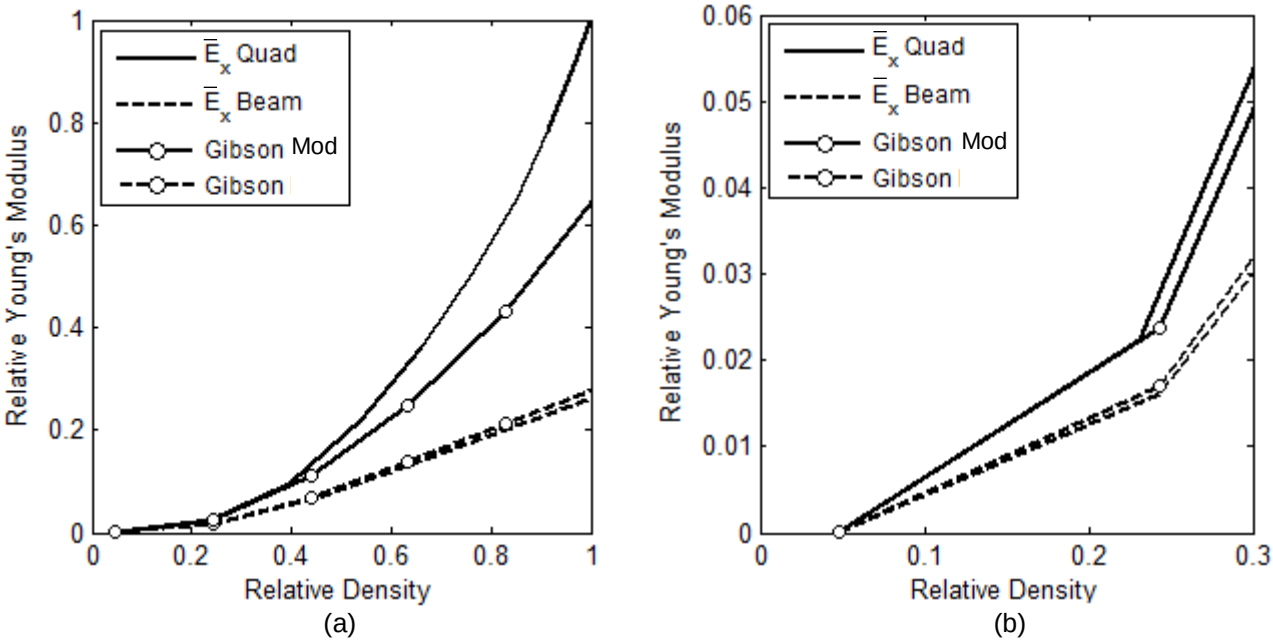

(a) (b)

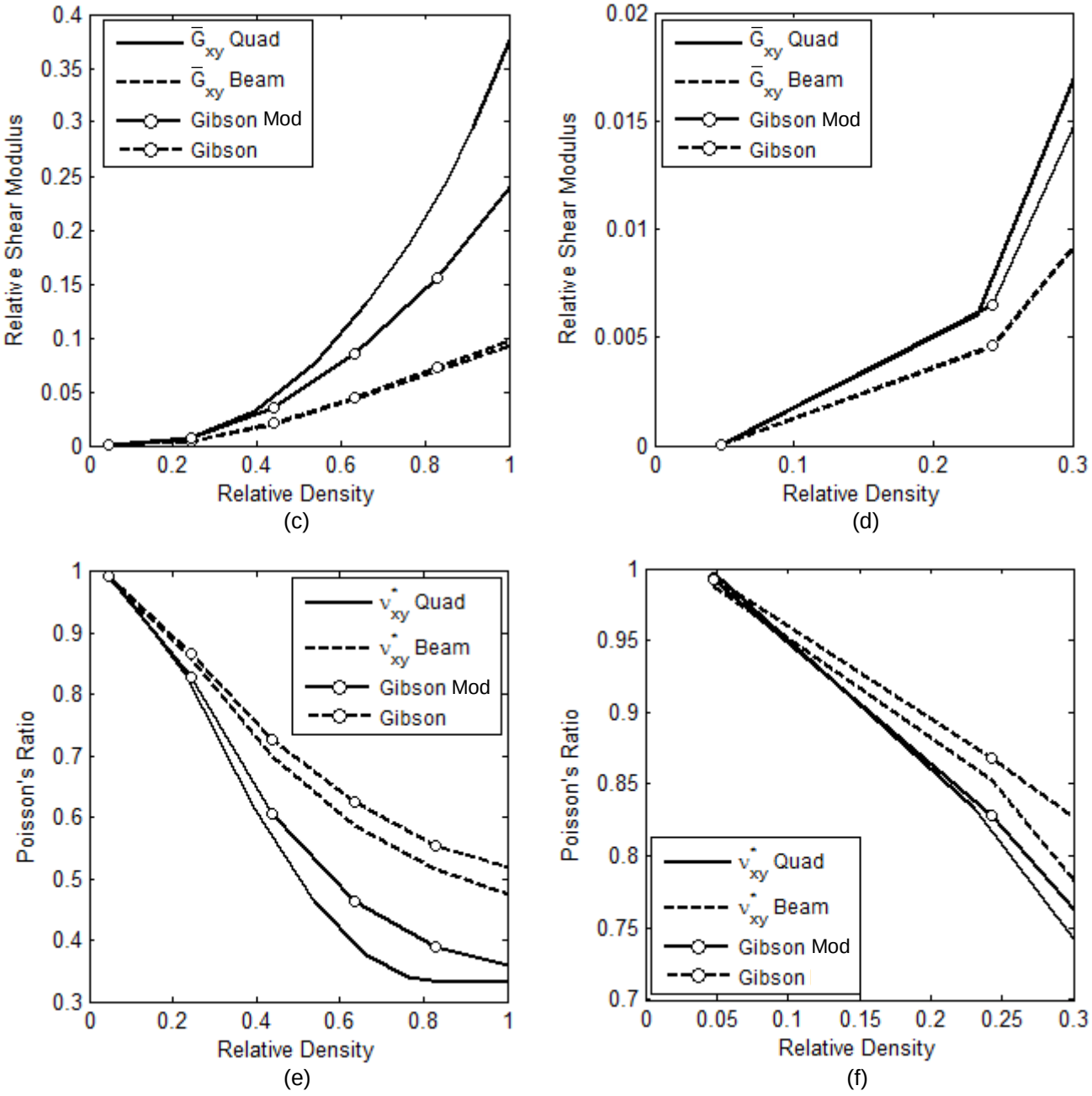

Figure 3-8 Comparison of quadrilateral plane strain elements and beam elements on the effective mechanical properties of regular, hexagonal honeycombs: (a) relative elastic modulus full scale and (b) magnified scale, (c) relative shear modulus full scale and (d) magnified scale, and (e) Poisson's ratio full scale and (f) magnified scale.

Observation of the plots reveals that the simple beam elements closely align with the unmodified Gibson equation; especially for relative densities below 0.3 as shown in the magnified plots. It has already been determined that the unmodified Gibson equation returns erroneous results. Thus, it can be stated that the use of CBEAM elements does not accurately capture the true global mechanical properties.

In addition to improperly calculating the effective material properties, the relative density is incorrectly calculated, as well. Studying Figure 3-8(b), (d), and (f), it is observed that the bend in the elastic modulus curve for the quadrilateral element model occurs at a relative density lower than that predicted by the modified Gibson equation. Reviewing Figure 3-4(b), the corners of the beam elements overlap. This mass overlap results in Gibson's equation for relative density (reference equation (11) in Section 3.1) overstating the relative density that actually exists. As the beam width increases, the mass overlap increases; thus, increasing the overstatement. For the hexagonal honeycomb described in Section 2.2, Gibson's equation for relative density achieves a value of 0.3 when the wall thickness is 6.3 units. At this wall thickness, the actual relative density is slightly over 2.8; resulting in an overestimation of 6.7%. This phenomenon was also acknowledged by Joshi [28] who created two-dimensional meshes of auxetic chiral honeycombs. His investigation consisted of comparing the in-plane effective material properties of a hexa-chiral structure modeled with two-dimensional plane stress quadrilateral elements against the same structure modeled via Timoshenko beam elements. His concluded that the quadrilateral element model produced accurate results whereas the Timoshenko beam model did not.

While the simple beam element modeling approach is not ideal, the time-savings is enormous. Using quadrilateral elements introduces several labor-intensive hurdles. For instance, unique models must be created for each relative density. Each wall thickness

requires the creation of a two-dimensional surface that must be properly meshed. As a result, each model has a different element and node numbering scheme. Therefore, each model requires the analyst to select the appropriate nodes when applying the loads and boundary conditions. These obstacles are not present in the beam model since the wall thicknesses are handled in the beam property set. Therefore, only one model is required which contains the curves making up the centerlines of the honeycomb walls. The analyst only has to mesh the curves and apply the loads and boundary conditions one time. Subsequent relative densities are analyzed by creating a new property set and applying it to the existing CBEAM elements. For the present thesis, the beam model and all property sets were created in less time than it took to mesh the geometry in Figure 2-10(j). In addition to faster modeling times, analysis of the beam models is significantly faster. The beam models run faster due to the simplicity of the beam element and the small number of beam elements required. For comparison, the mesh for the regular honeycomb in Figure 2-10(j) required over 283,000 quadrilateral elements and over 376,000 nodes. Using beam elements, only 9,180 elements and 10,488 nodes were required. Also, post processing the results is remarkably faster for the beam model. Since node numbering does not change, extracting the forces and displacements at the desired nodes is simplified. Therefore, it is left to the reader's discretion whether the more accurate results of the quadrilateral elements outweigh the significantly longer modeling times.

Chapter 4

Anisotropic Analysis

4.1 Finite Element Analysis Results

The anisotropic properties in Table 2-4 are applied to the specimens that have a wall thickness of 25.6 units and smaller (reference Table 2-1 for regular honeycombs and Table 2-2 for irregular honeycombs). This corresponds to specimens where the cellular structure is 40% to 100% developed. Comparing the geometries of the irregular honeycomb at 20% and 30% development, Figure 2-11(b) and Figure 2-11(c) in Section 2.2, it is apparent that not all of the nucleation points have formed for the specimen at 20% development. For the specimen at 30% development, the voids are extremely small which results in virtually nonexistent cell walls. Therefore, the anisotropic properties are applied to specimens at 40% to 100% development.

The finite element analysis results are shown in Figure 4-1 through Figure 4-6. Figure 4-1 through Figure 4-3 correspond to the regular honeycomb (δ = 1) and Figure 4-4 through Figure 4-6 correspond to the irregular honeycomb (δ = 0.75). Additionally, all of the results are tabulated in Appendix B. In each figure, the solid red line represents the property Case 1, where E_{sx} is twice E_{sy}, and the dashed black line represents the property Case 2, where E_{sy} is twice E_{sx}. For comparison purposes, the isotropic result, where E_{sx} is equal to E_{sy}, is represented by the solid black line. Since Gibson et al. [19, 37, 38] maintains that their formulations are applicable up to relative densities of 0.3, these portions of the figures are magnified, similar to the presentation of data in Figure 3-8.

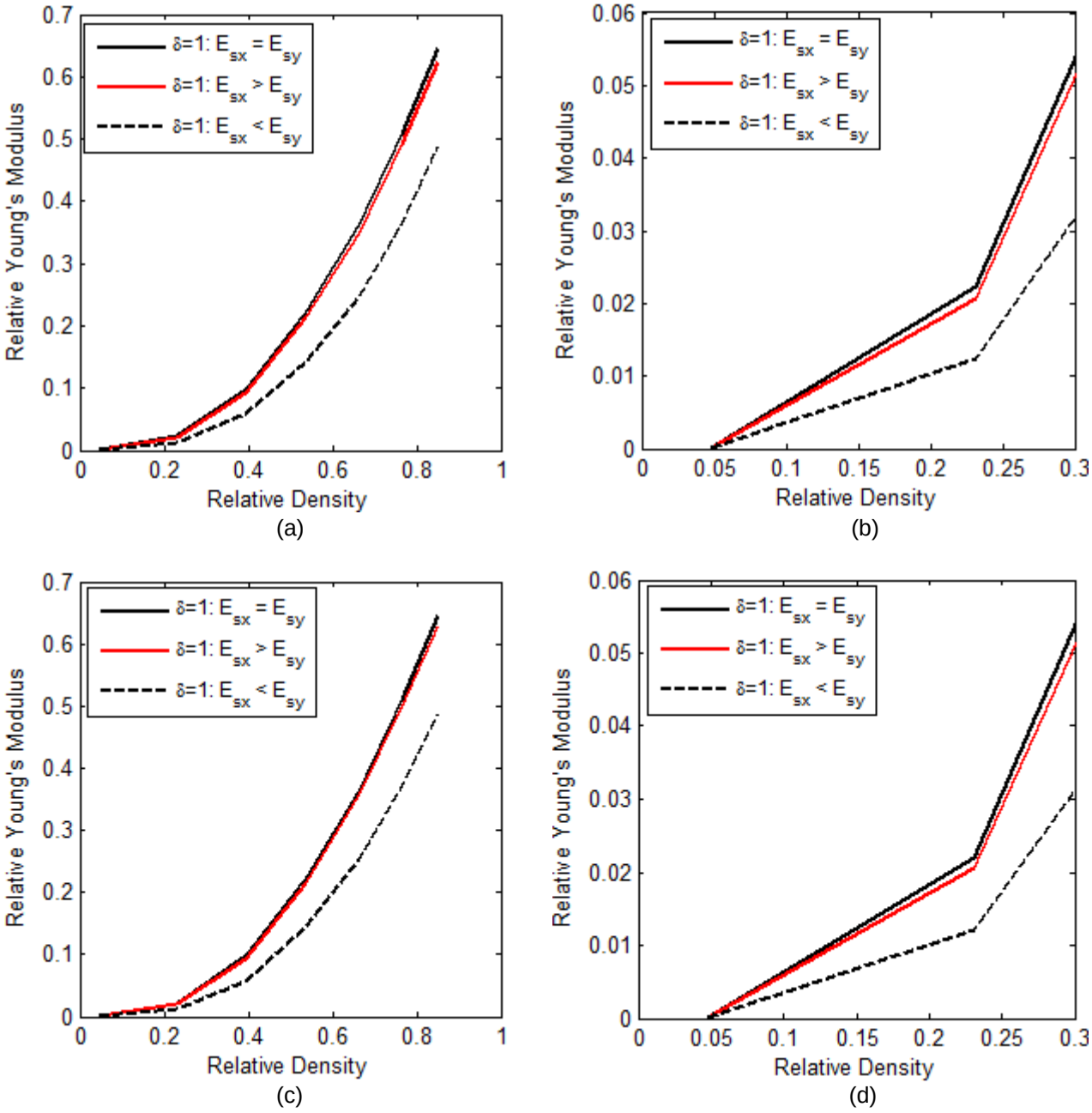

Figure 4-1 Relative Young's modulus vs relative density for a regularity of δ = 1: (a) $\bar{E}_x$ full scale and (b) $\bar{E}_x$ magnified scale, and (c) $\bar{E}_y$ full scale and (d) $\bar{E}_y$ magnified scale

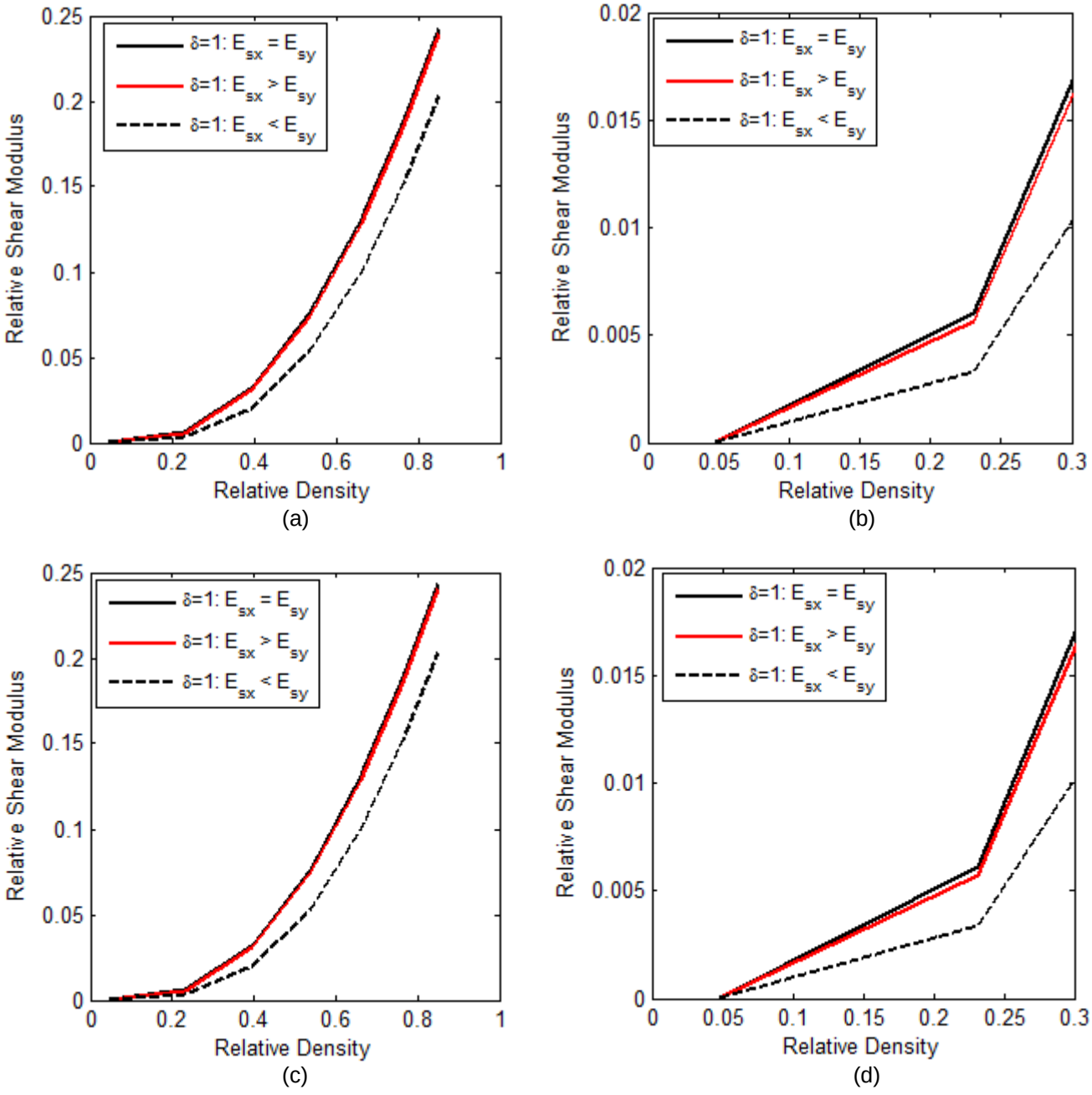

Figure 4-2 Relative shear modulus vs relative density for a regularity of δ = 1: (a) $\bar{G}_{xy}$ full scale and (b) $\bar{G}_{xy}$ magnified scale, and (c) $\bar{G}_{yx}$ full scale and (d) $\bar{G}_{yx}$ magnified scale

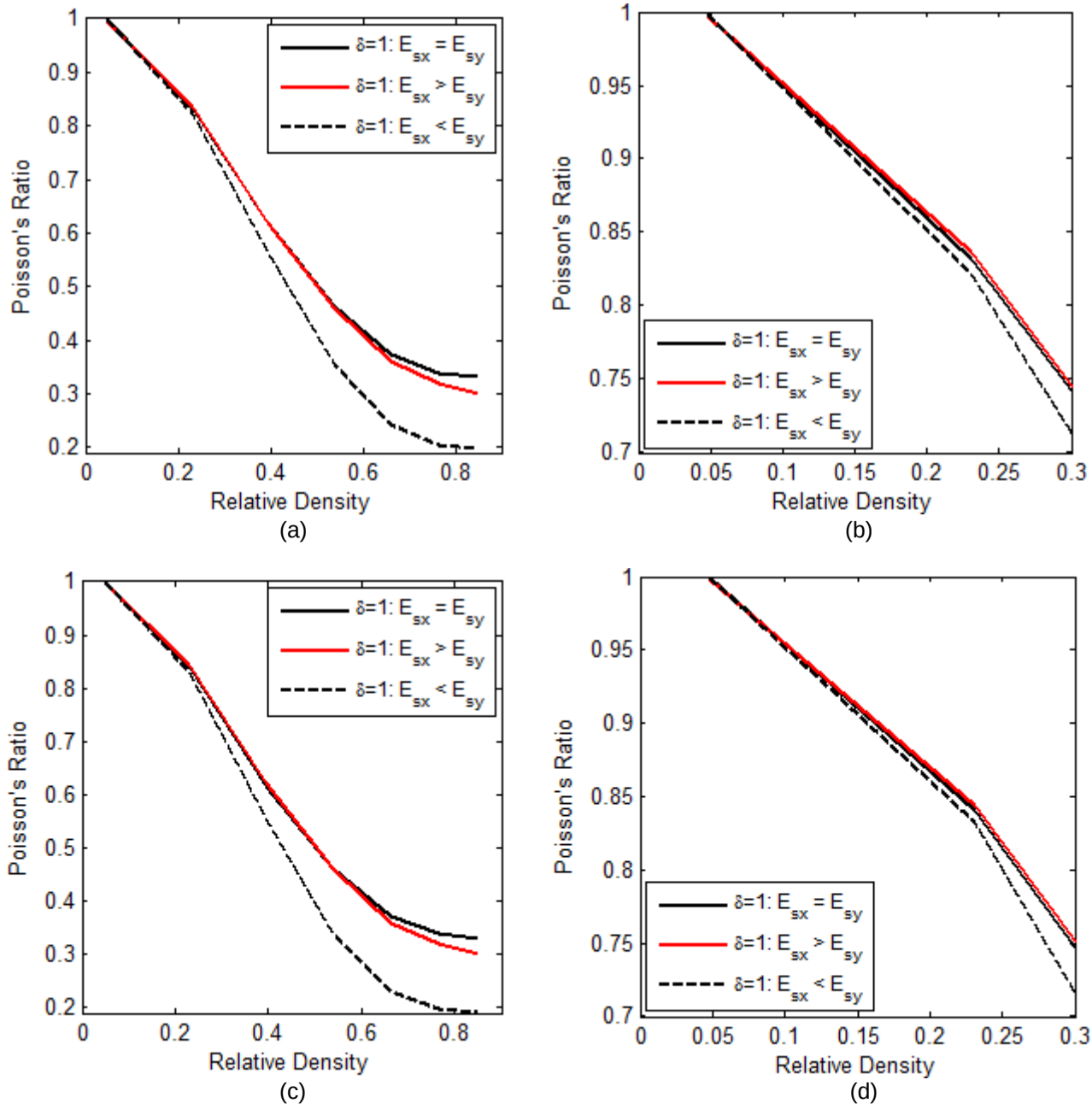

Figure 4-3 Poisson's ratio vs relative density for a regularity of δ = 1: (a) ν_{xy}^{*} full scale and (b) ν_{xy}^{*} magnified scale, and (c) ν_{yx}^{*} full scale and (d) ν_{yx}^{*} magnified scale

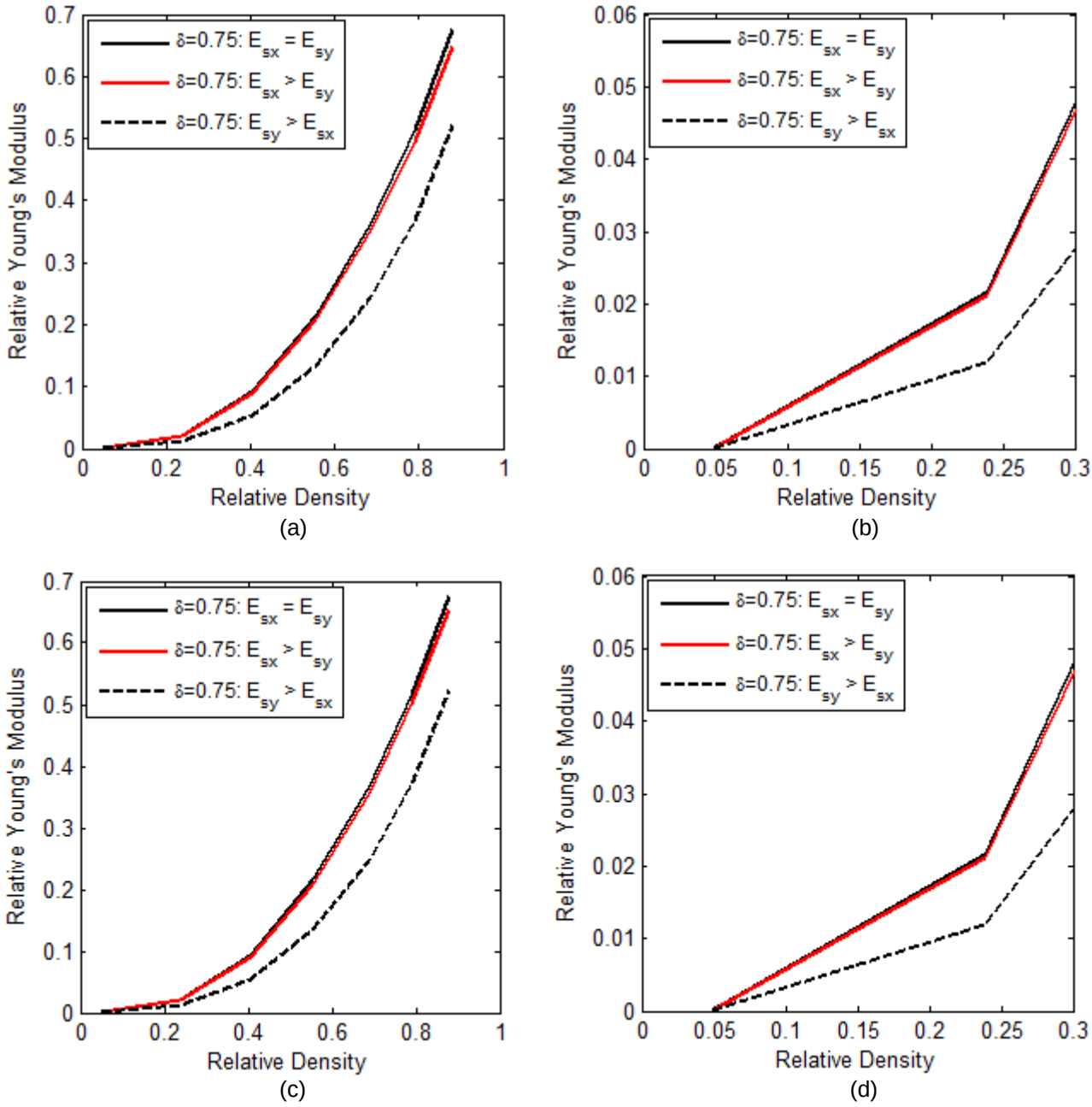

Figure 4-4 Relative Young's modulus vs relative density for a regularity of δ = 0.75: (a) $\bar{E}_x$ full scale and (b) $\bar{E}_x$ magnified scale, and (c) $\bar{E}_y$ full scale and (d) $\bar{E}_y$ magnified scale

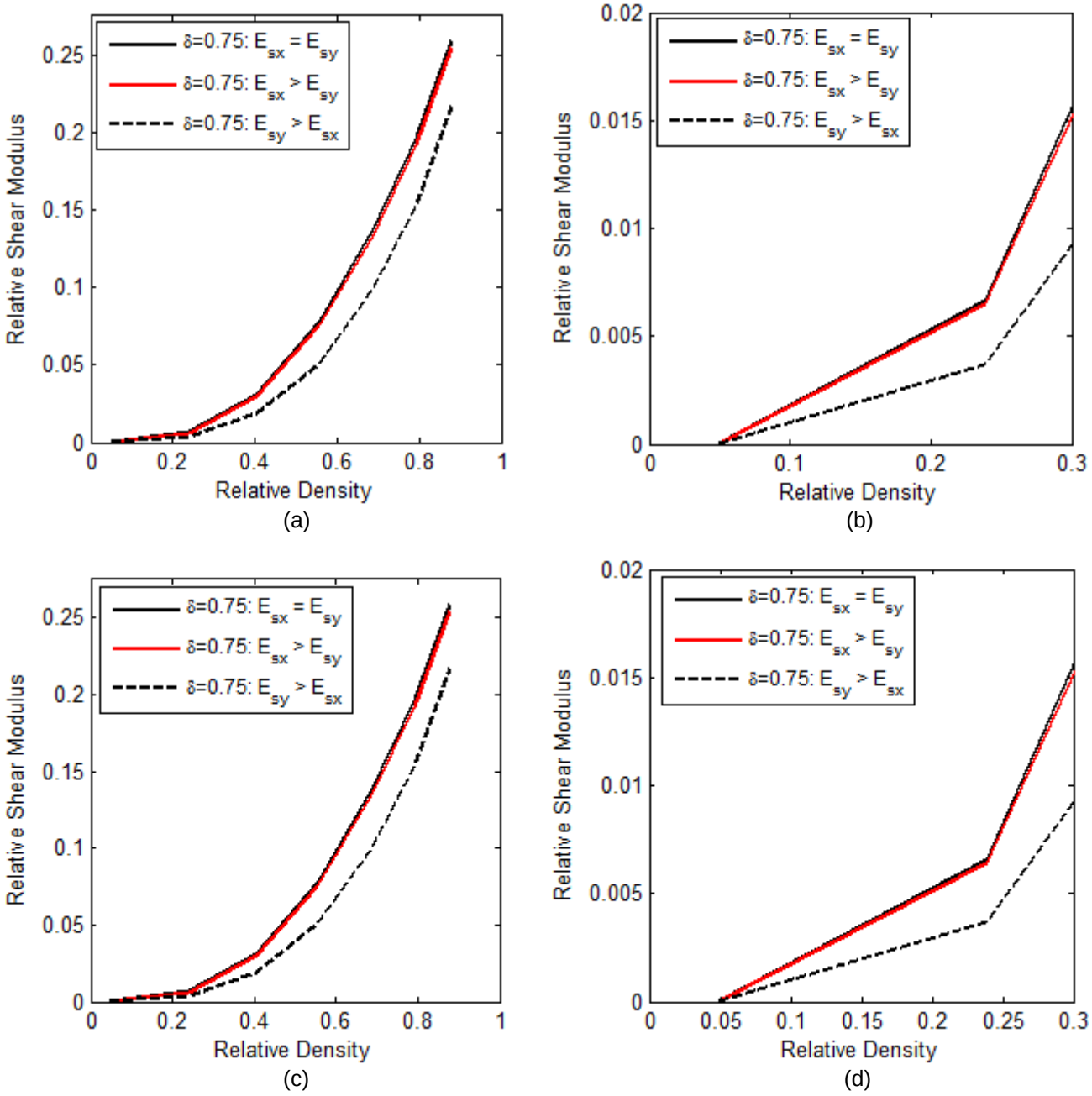

Figure 4-5 Relative shear modulus vs relative density for a regularity of δ = 0.75: (a) $\bar{G}_{xy}$ full scale and (b) $\bar{G}_{xy}$ magnified scale, and (c) $\bar{G}_{yx}$ full scale and (d) $\bar{G}_{yx}$ magnified scale

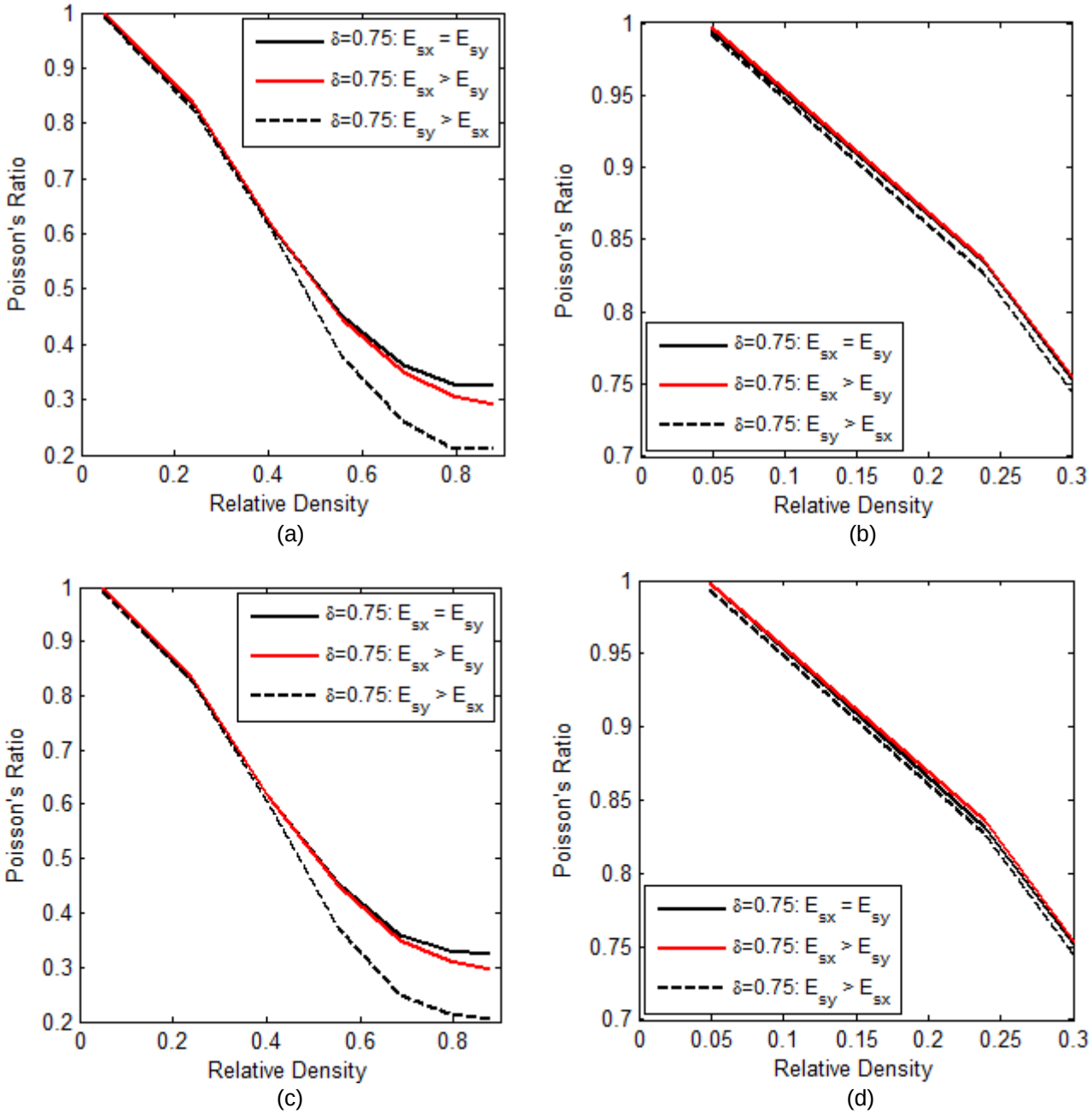

Figure 4-6 Poisson's ratio vs relative density for a regularity of δ = 0.75: (a) ν_{xy}^{*} full scale and (b) ν_{xy}^{*} magnified scale, and (c) ν_{yx}^{*} full scale and (d) ν_{yx}^{*} magnified scale

Similar to the isotropic results presented in Figure 3-2, the loading direction has minimal impact on the global mechanical properties for both the regular and irregular

arrangements. This relationship is applicable to both property Cases 1 and 2 and is observed by comparing plots (a) and (c) for each figure. While the impact of loading direction is minimal, the lower relative densities exhibited the largest variations in properties. For both property Cases 1 and 2, the regular arrangement at a relative density of 0.048 had the following property variations: $\bar{E}_x$ and $\bar{E}_y$ varied by 3.0%, $\bar{G}_{xy}$ and $\bar{G}_{yx}$ varied by 2.0%, and ν^*_{xy} and ν^*_{yx} varied by 1%. For both property Cases 1 and 2, the irregular arrangement at a relative density of 0.049 had the following property variations: $\bar{E}_x$ and $\bar{E}_y$ vary by 2%, $\bar{G}_{xy}$ and $\bar{G}_{yx}$ vary by 2%, and ν^*_{xy} and ν^*_{yx} vary by 1%. Therefore, it is proposed that the effective mechanical properties are not dependent on load direction for regular and irregular honeycombs with microstructural anisotropic properties (i.e. $\bar{E}_x$ = $\bar{E}_y$, $\bar{G}_{xy}$ = $\bar{G}_{yx}$, and ν^*_{xy} = ν^*_{yx}).

It is interesting to compare the properties of the anisotropic specimens to the isotropic specimens. Recall that for property Case 1, E_{sy} and ν_{syx} are half the value of E_{sx} and ν_{sxy}. Observing the Case 1 properties in Figure 4-1(a) and (c) and Figure 4-2(a) and (c), the Young's and shear moduli for the anisotropic specimens are up to 7% lower than their isotropic counterparts. Referencing Figure 4-3(a) and (c), the Poisson's ratio is up to 10% lower than the isotropic specimens. The same observations are made for the irregular honeycombs in Figure 4-4(a) and (c), Figure 4-5(a) and (c), and Figure 4-6(a) and (c). For the Case 1 properties, the Young's and shear moduli are up to 4% lower and the Poisson's ratio is up to 9% lower than the isotropic specimens. Recall from Section 3.1 that cell wall bending is the primary source of deformation and the contributions from axial and shear deformations are minimal. Per Silva et al. [38], axial and shear deformation constitute approximately 10% of the total deformation for a regular, hexagonal honeycomb with a relative density of 0.15. The results previously discussed substantiate Silva's et al. findings since the effective properties varied by no

more than 10% due to the 50% reduction in material properties in the elemental shear direction (i.e. lateral direction).

Recall that for property Case 2, E_{sx} and v_{sxy} are half the value of E_{sy} and v_{syx}. Observing the Case 2 properties in Figure 4-1(a) and (c) and Figure 4-2(a) and (c), the Young's and shear moduli for the anisotropic specimens are nearly 50% lower than their isotropic counterparts for a relative density of 0.048. As the relative density increases, the anisotropic specimens are 25% lower than the isotropic specimens. As the relative density increases, the amount of variation narrows. This is due to the fact the elements making up the junction do not belong to a specific ligament and therefore, are not assigned anisotropic properties. Instead, they retain the isotropic properties used for the isotropic models. Thus, as relative density increase, the anisotropic models become more and more similar to the isotropic models and the amount of variation in the effective properties reduces. Referencing Figure 4-3(a) and (c), the Poisson's ratio is less than 1% lower than the isotropic specimen for a relative density of 0.048. As the relative density increases, the Poisson's ratios are up to 40% lower than the isotropic models. This is attributed to v_{sxy} being half the value of v_{syx}. It is therefore concluded that the microstructural Poisson's ratio becomes more prevalent as the relative density increases and the specimen transitions from a cellular structure to a solid, porous structure.

The same observations are made for the irregular honeycombs in Figure 4-4(a) and (c), Figure 4-5(a) and (c), and Figure 4-6(a) and (c). For the Case 2 properties, the Young's and shear moduli for the anisotropic specimens are nearly 48% lower than their isotropic counterparts for a relative density of 0.049. As the relative density increases, the anisotropic specimens are 23% lower than the isotropic specimens. For a relative density of 0.049, the Poisson's ratio is less than 1% lower than the isotropic specimen. As the relative density increases, the Poisson's ratios are up to 35% lower than the isotropic

models. The significant change in the effective mechanical properties indicates that the material properties in the longitudinal elemental direction dominate the model behavior. It therefore can be said that the material properties in elemental lateral direction, i.e., the shear direction, have minimal impact on the effective mechanical properties.

Chapter 5

Conclusion

This thesis demonstrated the usefulness of the finite element method in obtaining the effective mechanical properties of regular, hexagonal honeycombs and irregular, Voronoi honeycombs. Finite element models were developed to explore the effective mechanical properties of honeycomb structures for isotropic and anisotropic microstructural material properties. The finite element models varied in relative density from purely solid to purely cellular to better understand the ranges of relative densities where a structure behaves as a cellular structure versus a porous solid.

The isotropic finite element analysis revealed that a theoretical solution that accurately determines the global mechanical properties across the full range of relative densities does not exist. It was determined that the current theoretical methods of porous media are sufficient in predicting the effective material properties for high relative densities for regular, hexagonal honeycombs and irregular, Voronoi honeycombs. For low relative densities, a modification to the ligament length parameter is proposed to improve Gibson and Ashby's [19] theoretical formulations for regular, hexagonal honeycombs. The aforementioned modification improves the correlation between the theoretical analysis and the finite element analysis and it expands the range of applicable relative densities beyond the 0.3 limit recommended by Gibson and Ashby. It was shown that there exists a range of relative densities where neither the theoretical analysis of honeycombs nor the theoretical analysis of porous media accurately predicts the effective mechanical properties. For this region, the finite element method is recommended. It was determined that the irregular honeycomb was stiffer than the regular honeycomb which is in good agreement with the relevant literature. It was also determined that the prevalent

method of modeling honeycombs with Timoshenko beam elements does not predict the effective mechanical properties as accurately as using two-dimensional, isoparametric plane strain elements. It is noted that the increased accuracy of the two-dimensional plane stain elements comes at the expense of significantly longer modeling and analysis times.

The anisotropic finite element analysis revealed that, similar to the isotropic models, the effective mechanical properties are not dependent on the loading direction (i.e. $\bar{E}_x = \bar{E}_y$, $\bar{G}_{xy} = \bar{G}_{yx}$, and $\nu^*_{xy} = \nu^*_{yx}$). The anisotropic analysis also revealed that the material properties in the longitudinal elemental direction dominated the model behavior for the regular, hexagonal honeycombs and the irregular, Voronoi honeycombs. Silva, Hayes, and Gibson [38] state that bending is the predominant mode of deformation and the axial and shear deformations are less significant. Similarly, it is concluded that material properties in the elemental longitudinal direction dominate the model behavior while the material properties in the elemental lateral direction (i.e. shear direction) play a less significant role. Therefore, the additive manufacturing processes are of the upmost importance since the anisotropy between the travel direction and build direction can significantly alter effective mechanical properties of cellular structures.

It is recommended that future work should expand the modeling techniques and microstructural anisotropy to three-dimensional foams. The research could also be expanded by studying the effects of microstructural anisotropy on the bulk modulus. The relationships observed via the finite element analysis should be substantiated through testing. This could be accomplished by using additive manufacturing techniques to fabricate the cellular structures for different build directions.

Appendix A

MATLAB® and NX SNAP™ Software Codes

1. MATLAB® code used to generate points in 2D space, via the simple sequential inhibition process [31], and construct the Voronoi diagram.

```
% Dist. btwn nuclei in hexagonal array is 42
d = 0.75*42;

% Get the vertices for the regions.
rx = [-48.5 825.03 825.03 -48.5 -48.5];
ry = [-63 -63 903 903 -63];
rx1 = [0 776.54 776.54 0 0];
ry1 = [0 0 840 840 0];
n = 588;
X = zeros(n,2);

% Generate the first event.
X(1,:) = csbinproc(rx,ry,1);
i = 1;

% Generate the other events.
while i<n
    [sx,sy] = csbinproc(rx, ry, 1);
    xt = [sx sy ; X(1:i,:)];
    % Find the distance between the events
    dist = pdist(xt);
    % Find the distance between the candidate event
    % and the others that have been generated already.
    ind = find(dist(1:i) <= d);
    if isempty(ind)
        % Then we keep the event.
        i = i+1
       X(i,:) = [sx, sy];
    end
end

%Plot nucleation points
xx=X(:,1); yy=X(:,2);
scatter(xx,yy,'.');
xxx=[0 776.54]; yyy=[0 0];
line(rx1,ry1)
axis([-100 1000 -100 1000])

% Construct the Voronoi Diagram
hold on
[v,c] = voronoin(X);
for j=1:length(c);
    nx{j}=v(c{j},:);
    %Plot Voronoi
    plot(nx{j}(:,1),nx{j}(:,2),'k')
```

```
    plot([nx{j}(1,1) nx{j}(length(nx{j}),1)],[nx{j}(1,2)…
        nx{j}(length(nx{j}),2)],'k')
end

plot(rx1,ry1,'k')
axis([0 1000 0 1000])
```

```
function [x,y] = csbinproc(xp, yp, n)
% CSBINPROC Generate homogeneous 2-D Poisson process.
% [X,Y] = CSBINPROC(XP,YP,N) This function generates a
% homogeneous 2-D Poisson process. Conditional on the number
% of data points N, this is uniformly distributed over the
% study region. The vectors XP and YP correspond to the x and y
% vertices of the study region. The vectors X and Y contain
% the locations for the generated events.
% EXAMPLE:
% xp = [0 1 1 0];  % vertices for region
% yp = [0 0 1 1];
% [X,Y] = csbinproc(xp,yp,100);
% plot(X,Y,'.')
% See also CSPOISSPROC, CSCLUSTPROC, CSINHIBPROC, CSSTRAUSPROC
% W. L. and A. R. Martinez, 9/15/01
% Computational Statistics Toolbox
x = zeros(n,1);
y = zeros(n,1);
i = 1;
% find the maximum and the minimum for a 'box' around
% the region. Will generate uniform on this, and throw
% out those points that are not inside the region.
minx = min(xp);
maxx = max(xp);
miny = min(yp);
maxy = max(yp);
cx = maxx-minx;
cy = maxy - miny;
while i <= n
    xt = rand(1)*cx + minx;
    yt = rand(1)*cy + miny;
    k = inpolygon(xt, yt, xp, yp);
    if k == 1
        % it is in the region
        x(i) = xt;
        y(i) = yt;
        i = i+1;
    end
end
```

2. Simple NX Application Programming (Siemens NX SNAP™ software [36]) code used to import the Voronoi diagram into Siemens NX™ software.

```
Option Explicit Off
Imports MiniSnap, MiniSnap.Create

Module SnapSample

Public Sub Main()

' Specimen boundary
b1=Point(0,0)
b2 = Point(776.54,0)
b3=Point(776.54,840)
b4=Point(0,840)
Line(b1,b2)
Line(b2,b3)
Line(b3,b4)
Line(b4,b1)

' Exclude unbounded pts outside this boundary
c1=Point(-50,-50)
c2 = Point(850,-50)
c3=Point(850,900)
c4=Point(-50,900)
Line(c1,c2)
Line(c2,c3)
Line(c3,c4)
Line(c4,c1)

'Each array element represents a Voronoi cell vertice
'Integer value represents the cell that the vertice belongs to
'1st and last element are the same vertice so the cell gets closed
'Cell 1 has 6 edges, Cell 2 has 5 edges, etc.
'Due to large size of array, not all values are shown
Dim Length As Integer() = {1, 1, 1, 1, 1, 1, 1, 2, 2, 2, 2, 2, 2,
...}

'X coordinate of Voronoi pts
'Due to large size of array, values are not shown
Dim Xvalues As Double() = {}

'Y coordinate of Voronoi pts
'Due to large size of array, values are not shown
Dim Yvalues As Double() = {}

For i =0 To 4076
  If Length(i)=Length(i+1)
```

```
    p1 = Point(Xvalues(i),Yvalues(i))
    p2 = Point(Xvalues(i+1),Yvalues(i+1))
    m=0
    n=0
    If i=0
      Line(p1,p2)
      Else
      For j=0 To i-1
        If Xvalues(i)=Xvalues(j) And Yvalues(i)=Yvalues(j)
          If Xvalues(i+1)=Xvalues(j+1) And Yvalues(i+1)=Yvalues(j+1)
            m=1
          End If
          If j>0
            ‘Eliminate ... and put entire IF statement on one line
            If Xvalues(i+1)=Xvalues(j-1) And ...
               Yvalues(i+1)=Yvalues(j-1)
              n=1
            End If
          End If
        End If
      Next
      If m=0 And n=0
        ‘Eliminate ... and put entire IF statement on one line
        If  Xvalues(i)>=0 And Xvalues(i)<=776.54 And ...
            Yvalues(i)>=0 And Yvalues(i)<=840 Or ...
            Xvalues(i+1)>=0 And Xvalues(i+1)<=776.54 And ...
            Yvalues(i+1)>=0 And Yvalues(i+1)<=840

          Line(p1,p2)
        End If
      End If
    End If
  End If
next

End Sub
End Module
```

Appendix B

Results

Table B-1 Isotropic results for honeycomb with regularity δ = 1.0

$\bar{\rho}$	$\bar{E}_1$	$\bar{E}_2$	$\bar{G}_{12}$	$\bar{G}_{21}$	ν_{12}^*	ν_{21}^*
0.048	1.69E-04	1.72E-04	4.25E-05	4.34E-05	0.9976	0.9991
0.231	2.23E-02	2.20E-02	6.01E-03	6.08E-03	0.8325	0.8408
0.395	0.0973	0.0980	0.0318	0.0320	0.6179	0.6167
0.538	0.2215	0.2230	0.0768	0.0770	0.4636	0.4623
0.662	0.3615	0.3627	0.1320	0.1323	0.3745	0.3719
0.766	0.5083	0.5093	0.1887	0.1891	0.3396	0.3385
0.850	0.6475	0.6470	0.2429	0.2433	0.3319	0.3311
0.916	0.7846	0.7826	0.2947	0.2950	0.3305	0.3303
0.963	0.8991	0.8993	0.3377	0.3379	0.3311	0.3305
0.991	0.9728	0.9734	0.3655	0.3655	0.3311	0.3301

Table B-2 Anisotropic Case 1 results for honeycomb with regularity δ = 1.0

$\bar{\rho}$	$\bar{E}_1$	$\bar{E}_2$	$\bar{G}_{12}$	$\bar{G}_{21}$	ν_{12}^*	ν_{21}^*
0.048	1.60E-04	1.70E-04	4.21E-05	4.29E-05	0.997	0.999
0.231	2.07E-02	2.07E-02	5.61E-03	5.69E-03	0.836	0.845
0.395	0.0935	0.0930	0.0306	0.0308	0.6201	0.6218
0.538	0.2137	0.2157	0.0744	0.0746	0.4583	0.4629
0.662	0.3495	0.3572	0.1290	0.1292	0.3595	0.3591
0.766	0.4919	0.4981	0.1855	0.1858	0.3301	0.3216
0.850	0.6245	0.6285	0.2402	0.2404	0.3060	0.2995

Table B-3 Anisotropic Case 2 results for honeycomb with regularity δ = 1.0

$\bar{\rho}$	$\bar{E}_1$	$\bar{E}_2$	$\bar{G}_{12}$	$\bar{G}_{21}$	ν_{12}^*	ν_{21}^*
0.048	8.49E-05	8.78E-05	2.19E-05	2.23E-05	0.998	1.000
0.231	1.24E-02	1.21E-02	3.31E-03	3.35E-03	0.822	0.832
0.395	0.0590	0.0579	0.0200	0.0196	0.5633	0.5537
0.538	0.1430	0.1442	0.0539	0.0539	0.3551	0.3407
0.662	0.2471	0.2518	0.1006	0.1005	0.2441	0.2305
0.766	0.3665	0.3729	0.1524	0.1525	0.2034	0.1989
0.850	0.4887	0.4877	0.2030	0.2034	0.1979	0.1923

Table B-4 Isotropic results for honeycomb with regularity δ = 0.75

$\bar{\rho}$	$\bar{E}_1$	$\bar{E}_2$	$\bar{G}_{12}$	$\bar{G}_{21}$	ν_{12}^*	ν_{21}^*
0.049	1.87E-04	1.90E-04	5.06E-05	5.15E-05	0.9943	0.9986
0.239	2.16E-02	2.16E-02	6.64E-03	6.59E-03	0.8349	0.8313
0.405	0.0929	0.0932	0.0310	0.0311	0.6131	0.6128
0.554	0.2146	0.2147	0.0770	0.0771	0.4507	0.4543
0.686	0.3631	0.3647	0.1365	0.1375	0.3627	0.3604
0.791	0.5144	0.5162	0.1965	0.1968	0.3271	0.3292
0.879	0.6762	0.6774	0.2592	0.2594	0.3254	0.3238
0.942	0.8391	0.8437	0.3195	0.3196	0.3238	0.3214
0.981	0.9512	0.9517	0.3581	0.3582	0.3309	0.3306
0.996	0.9904	0.9905	0.3718	0.3718	0.3330	0.3324

Table B-5 Anisotropic Case 1 results for honeycomb with regularity δ = 0.75

$\bar{\rho}$	$\bar{E}_1$	$\bar{E}_2$	$\bar{G}_{12}$	$\bar{G}_{21}$	ν_{12}^*	ν_{21}^*
0.049	1.84E-04	1.86E-04	5.00E-05	5.08E-05	0.997	0.998
0.239	2.10E-02	2.11E-02	6.48E-03	6.43E-03	0.837	0.835
0.405	0.0902	0.0906	0.0301	0.0302	0.6155	0.6129
0.554	0.2078	0.2078	0.0747	0.0748	0.4468	0.4501
0.686	0.3509	0.3553	0.1330	0.1339	0.3509	0.3485
0.791	0.4959	0.5000	0.1924	0.1928	0.3152	0.3126
0.879	0.6502	0.6544	0.2548	0.2549	0.2976	0.2958

Table B-6 Anisotropic Case 2 results for honeycomb with regularity δ = 0.75

$\bar{\rho}$	$\bar{E}_1$	$\bar{E}_2$	$\bar{G}_{12}$	$\bar{G}_{21}$	ν_{12}^*	ν_{21}^*
0.049	9.64E-05	9.76E-05	2.60E-05	2.67E-05	0.992	0.993
0.239	1.19E-02	1.19E-02	3.69E-03	3.66E-03	0.827	0.827
0.405	0.0548	0.0552	0.0188	0.0188	0.6059	0.6007
0.554	0.1349	0.1349	0.0509	0.0509	0.3777	0.3720
0.686	0.2438	0.2461	0.0986	0.0992	0.2601	0.2495
0.791	0.3691	0.3703	0.1532	0.1535	0.2110	0.2127
0.879	0.5227	0.5232	0.2169	0.2170	0.2154	0.2061

Table B-7 Isotropic results for honeycomb with regularity δ = 1.0 using Timoshenko beam elements

$\bar{\rho}$	$\bar{E}_1$	$\bar{E}_2$	$\bar{G}_{12}$	$\bar{G}_{21}$	ν_{12}^*	ν_{21}^*
0.048	1.56E-04	1.74E-04	4.07E-05	4.06E-05	0.9907	1.0225
0.231	1.61E-02	1.73E-02	4.59E-03	4.58E-03	0.8597	0.8873
0.395	0.0643	0.0681	0.0200	0.0199	0.7003	0.7190
0.538	0.1294	0.1360	0.0429	0.0428	0.5868	0.6007
0.662	0.1992	0.2084	0.0688	0.0687	0.5155	0.5273
0.766	0.2694	0.2809	0.0956	0.0955	0.4706	0.4816
0.850	0.3387	0.3525	0.1224	0.1222	0.4414	0.4520
0.916	0.4070	0.4231	0.1488	0.1486	0.4216	0.4321
0.963	0.4744	0.4927	0.1749	0.1747	0.4078	0.4182
0.991	0.5410	0.5615	0.2008	0.2005	0.3977	0.4081

Appendix C

Nomenclature

A	Finite area in the SSI process
API	Application Programming Interface
c	Voronoi cell output array for [v,c] = voronoin(x) function
C	Circle constraint for the Delaunay tessellation
CAD	Computer-Aided Design
CBEAM	One-dimensional simple beam element
CQUAD4	Isoparametric plane strain quadrilateral shell element
CTRIA3	Isoparametric plane strain triangular shell element
d	Disk diameter in the SSI process (i.e. inhibition distance)
d_{max}	Maximum disk diameter for regular arrangement in SSI process
E_s	Elastic modulus of solid material
E*	Elastic modulus of cellular material
$\bar{E}$	Relative elastic modulus – the ratio of E* to Es
FEM	Finite element model
G_s	Shear modulus of solid material
G*	Shear modulus of cellular material
$\bar{G}$	Relative shear modulus – the ratio of G* to Gs
GUI	Graphical User Interface
h_w	Internal cell height
l	Ligament length
n	Number of disks in SSI process or number of points (i.e. disk centers) or Number of holes in a unit area in Poisson's equation for porous media
PSHELL	Property entry for CQUAD4 and CTRIA3 shell elements
rx	Array containing the x-coordinates of the boundary vertices
ry	Array containing the y-coordinates of the boundary vertices

SSI	Simple Sequential Inhibition process
SNAP™	Simple NX Application Programming
t_w	Thickness of cell wall
v	Voronoi vertice output array for [v,c] = voronoin(x) function
x	Nuclei point input array for [v,c] = voronoin(x) function
γ	Shear strain
α	Adjustable parameter in Poisson's equation for porous media
δ	Regularity – ratio of d to d_{max}
ε	Tensile strain
η	Packing density
θ	Angle of cell wall relative to the horizontal axis
ν_s	Poisson's ratio of solid material
ν^*	Poisson's ratio of cellular material
ρ_c	Percolation threshold – 1 - η
ρ_s	Density of solid material
ρ^*	Density of cellular material
$\bar{\rho}$	Relative density – the ratio of ρ^* to ρ_s
σ	Tensile stress
τ	Shear stress

References

1. ASM Handbook, Vol. 2. Properties and Section: Nonferrous Alloys and Special-Purpose Materials, ASM International (1990): 62-122.
2. Aurenhammer, Franz and Rolf Klein., "Voronoi Diagrams." *Handbook of Computational Geometry* Chapter 5 (2000): 201-290.
3. Benveniste, Y., "A New Approach to the Application of Mori-Tanaka's Theory in Composite Materials." *Mechanics of Materials* Vol 6 (1987): 147-157.
4. Budiansky, B., "On the Elastic Moduli of Some Heterogeneous Materials." *Journal of the Mechanics and Physics of Solids* Vol 13 (1965): 223-227.
5. Busson, Anthony and Chelius, Guillaume., "Capacity and Interference Modeling of CSMA/CA Networks Using SSI Point Processes." *Telecommunication Systems* Vol 57, No. 1 (2014): 25-39.
6. Chen, C., Lu, T.J. and Fleck, N.A., "Effect of Imperfections on the Yielding of Two-Dimensional Foams." *Journal of the Mechanics and Physics of Solids* Vol 47 (1999): 2235-2272.
7. Christensen, R. M. and K. H. Lo, "Solutions for Effective Shear Properties in Three Phase Sphere and Cylinder Models." *Journal of the Mechanics and Physics of Solids* Vol 27 (1979): 315-330.
8. Christodoulou, P.J. Tan, "Crack Initiation and Fracture Toughness of Random Voronoi Honeycombs." *Engineering Fracture Mechanics* Vol 104 (2013): 140-161.
9. Dai, Gaoming, and Weihong Zhang, "Cell Size Effect Analysis of the Effective Young's Modulus of Sandwich Core." *Computational Materials Science* Vol 46 (2009): 744-748.

10. Day, A. R., K. A. Snyder, E. J. Garboczi, and M. F. Thorpe, “The Elastic Moduli of a Sheet Containing Circular Holes.” *Journal of the Mechanics and Physics of Solids* Vol 40, No. 5 (1992): 1031-1051.
11. Diggle, Peter J., “On Parameter Estimation and Goodness-of-Fit Testing for Spatial Point Patterns.” *Biometrics* Vol 35, No. 1 (1979): 87-101.
12. Diggle, P. J., Besag, J. and Gleaves, J. T., “Statistical Analysis of Spatial Point Patterns by Means of Distance Methods.” *Biometrics* Vol 32, No. 3 (1976): 659-667.
13. Du, D. X. and Q. S. Zheng, “A Further Exploration of the Interaction Direct Derivation (IDD) Estimate for the Effective Properties of Multiphase Composites Taking Into Account Inclusion Distribution.” *Acta Mechanica* Vol 157 (2002): 61-80.
14. “Economic Values for FAA Investment and Regulatory Decisions, A Guide Final Report.” *FAA.gov*. U.S. Federal Aviation Administration, https://www.faa.gov/regulations_policies/policy_guidance/benefit_cost/media/econ-value-section-4-op-costs.pdf. Web.
15. Ferro, Greg. 14 July 2012. http://etherealmind.com/size-differences-cat5-and-cat6-cable-bundles/?share=twitter. Web.
16. Gálvez, Oscar Efraín Sotomayor. “Numerical Modeling of Random 2D and 3D Structural Foams Using Voronoi Diagrams: A Study of Cell Regularity and Compression Response.” MS Thesis. Auburn University, 2013.
17. Garboczi, E. J., M. F. Thorpe, M. S. DeVries, and A. R. Day, “Universal Conductivity Curve for a Plane Containing Random Holes.” *Physical Review A* Vol 43, No. 12 (1991): 6473-6482.
18. Gandhi, Ninad. “Finite Element Analysis of Effective Mechanical Properties of Hierarchical Honeycomb Structures.” MS Thesis. Clemson University, 2015.

19. Gibson, Lorna J. and Michael F. Ashby. Cellular Solids: Structure and Properties. Second edn. Cambridge University Press, 1997.
20. Gibson, L. J., M. F. Ashby, G. S. Schajer, and C. I. Robertson. “The Mechanics of Two-Dimensional Cellular Materials.” *Proceedings of the Royal Society of London. Series A, Mathematical and Physical Sciences* Vol 382, No. 1782 (1982): 25-42.
21. Harders, Harald, Knut Hupfer, and Joachim Rösler, “Influence of Cell Wall Shape and Density on the Mechanical Behaviour of 2D Foam Structures.” *Acta Materialia* Vol 53 (2005): 1335-1345.
22. Hashin, Z., “On Elastic Behaviour of Fibre Reinforced Materials of Arbitrary Transverse Phase Geometry.” *Journal of the Mechanics and Physics of Solids* Vol 13 (1965): 119-134.
23. Hashin, Z. and Rosen, B. W., “The Elastic Moduli of Fiber Reinforced Materials.” *ASME Journal of Applied Mechanics*, Vol 31 (1964): 223-232.
24. Hashin, Z. and S. Shtrikman, “A Variational Approach to the Theory of the Elastic Behaviour of Multiphase Materials.” *Journal of the Mechanics and Physics of Solids* Vol 11 (1963): 127-140.
25. HEXCEL Corporation. HexWeb™ Honeycomb Attributes and Properties: A Compressive Guide to Standard Hexcel Honeycomb Materials, Configurations, and Mechanical Properties. Hexcel, 1999.
26. Hu, N., B. Wang, G. W. Tan, Z. H. Yao, and W. F. Yuan, “Effective Elastic Properties of 2-D Solids with Circular Holes: Numerical Simulations.” *Composites Science and Technology* Vol. 60 (2000): 1811-1823.
27. Huang, Y., K. X. Hu, X. Wei, and A. Chandra, “A Generalized Self-Consistent Mechanics for Composite Materials with Multiphase Inclusions.” *Journal of the Mechanics and Physics of Solids* Vol 42, No. 3 (1994): 491-504.

28. Joshi, Hrishikesh, “Finite Element Analysis of Effective Mechanical Properties, Vibration and Acoustic Performance of Auxetic Chiral Core Sandwhich Structures.” *All Theses.* Paper 1723.
29. Klusemann, B. and B. Svendsen, “Homogenization Methods for Multi-Phase Elastic Composites: Comparisons and Benchmarks.” *Technische Mechanik* Vol 20, No. 4 (2010): 374-386.
30. “The Lightest Metal Ever.” *Boeing.com.* Boeing, 06 Oct. 2015 www.boeing.com/features/2015/10/innovation-lightest-metal-10-15.page. Web.
31. Martinez, Wendy L. and Angel R. Martinez. Computational Statistics Handbook with MATLAB®. Chapman & Hall/CRC, 2002.
32. Metalfoam. 23 May 2011. A photographic image of an aluminium foam sandwich produced by metalfoam company. https://commons.wikimedia.org/wiki/File:Aluminium_foam_sandwich.jpg. Web.
33. MSC Software®. MSC Nastran 2012 Linear Static Analysis User’s Guide. (2011).
34. Onck, P.R., E.W. Andrews, and L.J. Gibson, “Size Effects in Ductile Cellular Solids. Part I: Modeling.” *International Journal of Mechanical Sciences* Vol 43 (2001): 681-699.
35. Shen, Chen, Zengxi Pan, Dominic Cuiuri, Bosheng Dong, and Huijun Li, “In-depth Study of the Mechanical Properties for Fe_3Al Based Iron Aluminide Fabricated Using the Wire-Arc Additive Manufacturing Process.” *Materials Science & Engineering A* Vol 669 (2016): 118-126.
36. Siemens Product Lifecycle Management Software Inc. Getting Started with SNAP, Revision 10.0. (2014)

37. Silva, Matthew J., Lorna J. Gibson, “The Effects of Non-Periodic Microstructure and Defects on the Compressive Strength of Two-Dimensional Cellular Solids.” *International Journal of Mechanical Sciences* Vol 39, No. 5 (1997): 549-563.
38. Silva, Matthew J., Wilson C. Hayes and Lorna J. Gibson, “The Effects of Non-Periodic Microstructure on the Elastic Properties of Two-Dimensional Cellular Solids.” *International Journal of Mechanical Sciences* Vol 37, No. 11 (1995): 1161-1177.
39. Tables of Physical & Chemical Constants (16th edition 1995). 2.2.2 Elasticities and strengths. Kaye & Laby Online. Version 1.0 (2005) www.kayelaby.npl.co.uk
40. Taya, Minoru and Tsu-Wei Chou, “On Two Kinds of Ellipsoidal Inhomogeneities in an Infinite Elastic Body: An Application to a Hybrid Composite.” *International Journal of Solids and Structures* Vol 17 (1981): 553-563.
41. http://www.americasfencestore.com/product_images/r/021/Galvanized_Pipe__18523_zoom.jpg. Web.
42. Vajjhala, Surekha, “Finite Element Analysis of Voronoi Cellular Solids.” MS Thesis. Massachusetts Institute of Technology, 1996.
43. Wang, J.F., Q.J. Sun, H. Wang, J.P. Liu, and J.C. Feng, “Effect of Location on Microstructure and Mechanical Properties of Additive Layer Manufacture Inconel 625 Using Gas Tungsten Arc Welding.” *Materials Science & Engineering A* Vol 676 (2016): 395-405.
44. Wang, Zhuqing, Todd A. Palmer, Allison M. Beese, “Effect of Processing Parameters on Microstructure and Tensile Properties of Austenitic Stainless Steel 304L Made by Direct Energy Deposition Additive Manufacturing.” *Acta Materialia* Vol 110 (2016): 226-235.
45. Zheng, Q. S. and D. X. Du, “An Explicit and Universally Applicable Estimate for the Effective Properties of Multiphase Composites Which Accounts for Inclusion

Distribution." *Journal of the Mechanics and Physics of Solids* Vol 49 (2001): 2765-2788.

46. Zhu, H. X., J. R. Hobdell and A. H. Windle. "Effects of Cell Irregularity on the Elastic Properties of Open-Cell Foams." *Acta Metallurgica Inc*. Vol 48 (2000): 4893-4900.
47. Zhu, H. X., S. M. Thorpe and A. H. Windle. "The Effect of Cell Irregularity on the High Strain Compression of 2D Voronoi Honeycombs." *International Journal of Solids and Structures* Vol 43 (2006): 1061-1078.

Biographical Information

Justin Compton received his Bachelor of Science degree in Aerospace Engineering with honors cum laude from Texas A&M University in May 2012. He was the recipient of the Joanne and Edward “Pete” Aldridge ’60 Endowed Scholarship during his sophomore, junior, and senior years. During the summer of 2010 he worked as a software engineering intern for L3 Communications at the Johnson Space Center in Houston, Texas. For his senior design project, he, along with five other talented engineers, designed, built, and flew an unmanned aircraft. His senior design project was awarded the Stanley H. Lowy Award for best aircraft design. As a senior, he became a member of the Sigma Gamma Tau Aerospace Engineering Honors Society.

After graduating from Texas A&M University, he accepted employment with L3 Mission Integration in Greenville, Texas where he works as a stress analysis engineer. L3 Mission Integration generously funded his graduate studies through their educational assistance program. While working full time, he began his Master of Science degree in Aerospace Engineering at The University of Texas at Arlington in August 2013 as a distance education student. After completing his Master of Science degree in May 2017, he will continue to work as a stress analysis engineer for L3 Mission Integration.